Anatomy of an extensional shear zone in the mantle, Lanzo massif, Italy

Mary-Alix Kaczmarek, Andrea Tommasi

Geochemistry Geophysics Geosystems G3

Article
Volume 12, Number 8
10 August 2011
Q0AG06, doi:10.1029/2011GC003627
ISSN: 1525-2027

Published by AGU and the Geochemical Society

Anatomy of an extensional shear zone in the mantle, Lanzo massif, Italy

Mary-Alix Kaczmarek
Géosciences Montpellier, Université Montpellier 2 and CNRS, Place E. Bataillon, F-34095 Montpellier CEDEX 5, France

Now at Department of Applied Geology, Curtin University of Technology, GPO Box U1987, Perth, Western Australia 6845, Australia. (m.kaczmarek@curtin.edu.au)

Andréa Tommasi
Géosciences Montpellier, Université Montpellier 2 and CNRS, Place E. Bataillon, F-34095 Montpellier CEDEX 5, France

[1] Analysis of the microstructures in the km-scale mantle shear zone that separates the northern and the central parts of the Lanzo peridotite massif provides evidence of an evolution in time and space of deformation processes accommodating shearing in the shallow mantle within an extensional setting. This shear zone displays an asymmetric distribution of deformation facies. From south to north, gradual reorientation of the foliation of coarse porphyroclastic plagioclase-bearing peridotites is followed by development of protomylonites, mylonites, and mm-scale ultramylonite bands. A sharp grain size gradient marks the northern boundary. Early deformation under near-solidus conditions in the south is recorded by preservation of weakly deformed interstitial plagioclase and almost random clinopyroxene and plagioclase crystal orientations. Feedback between deformation and melt transport probably led to melt focusing and strain weakening in the shear zone. Overprint of melt-rock reaction microstructures by solid-state deformation and decrease in recrystallized grain size in the protomylonites and mylonites indicate continued deformation under decreasing temperature. Less enriched peridotite compositions and absence of ultramafic dykes or widespread melt-impregnation microstructures north of the shear zone and clinopyroxene and amphibole enrichment in the mylonites and ultramylonites suggest that the shear zone acted as both a thermal barrier and a high-permeability channel for late crystallizing fluids. These observations, together with chemical data indicating faster cooling of central Lanzo relative to the northern body, corroborate that this shear zone is a mantle detachment fault. All deformation facies have crystal preferred orientations consistent with deformation by dislocation creep with dominant activation of the (010)[100] and (100)[001] systems in olivine and orthopyroxene, respectively. Dynamic recrystallization produces dispersion of olivine CPO but not a change of dominant deformation mechanism. Evidence for activation of grain boundary sliding is limited to mm-scale ultramylonite bands, where solid-state reactions produced very fine grained polymineralic aggregates. Except for these latest stages of deformation, strain localization does not result from the microstructural evolution; the grain size decrease is a consequence of the need to deform a rock volume whose strength continuously increases because of decreasing temperature conditions. Strain localization in the intermediate levels thus essentially results from the more localizing behavior of both the deep, partially molten, and shallow parts of this extensional shear zone distribution.

Components: 11,800 words, 13 figures.

Keywords: dislocation creep; extension; grain boundary sliding; lithospheric thinning; melt; ultramylonite bands.

Index Terms: 3625 Mineralogy and Petrology: Petrography, microstructures, and textures.

Received 15 March 2011; **Revised** 24 May 2011; **Accepted** 25 May 2011; **Published** 10 August 2011.

Kaczmarek, M.-A., and A. Tommasi (2011), Anatomy of an extensional shear zone in the mantle, Lanzo massif, Italy, *Geochem. Geophys. Geosyst.*, *12*, Q0AG06, doi:10.1029/2011GC003627.

Theme: Oceanic Detachment Faults

1. Introduction

[2] Strain localization is observed at all scales in geological materials, from deformation bands within single grains up to lithospheric-scale shear zones [e.g., *Poirier*, 1980; *White et al.*, 1980; *Vissers et al.*, 1995; *Vauchez and Tommasi*, 2003; *Vauchez et al.*, 2005]. Several processes may interact to produce strain localization, from intrinsic plastic anisotropy of the crystals [*Durham and Goetze*, 1977; *Bai et al.*, 1991; *Tommasi et al.*, 2009], shear heating [e.g., *Regenauer-Lieb and Yuen*, 2003], grain size reduction due to dynamic recrystallization [*Braun et al.*, 1999] or reactions [*Newman et al.*, 1999], to lateral variations in the compositional stratification or thermal gradient within a plate [e.g., *Dunbar and Sawyer*, 1989; *Tommasi et al.*, 1995; *Vauchez et al.*, 1995; *Neves et al.*, 2008].

[3] At the sample scale, the presence of secondary phases may hinder grain growth, allowing for activation of diffusion-assisted grain boundary sliding [e.g., *Newman et al.*, 1999; *Stünitz and Tullis*, 2001; *Herwegh et al.*, 2005; *Skemer et al.*, 2010]. At larger scales, temperature gradients [e.g., *Vissers et al.*, 1995; *Précigout et al.*, 2007; *Soustelle et al.*, 2009] and presence of melt and/or fluids [e.g., *Tommasi et al.*, 1994; *Kelemen and Dick*, 1995; *Brown and Solar*, 1998; *Le Roux et al.*, 2008] are essential parameters influencing the rheology and, consequently, the deformation. Even small amounts of (interstitial) melt substantially decrease the rocks strength in both dislocation and diffusion creep regimes by forming interconnected fast diffusion paths and reducing contact areas between grains [*Hirth and Kohlstedt*, 1995a, 1995b]. Experiments also show that deformation induces melt segregation into an anastomozing network of melt-rich zones [*Holtzman et al.*, 2003]. This allows for further viscosity reduction and strain localization in the melt-rich zones [*Holtzman and Kohlstedt*, 2007].

[4] In this paper we present a detailed study of the deformation distribution and associated microstructures in a section across a well-exposed 1 km wide mantle shear zone in the Lanzo peridotite massif, Western Alps (Italy). We analyzed the microstructures and crystallographic preferred orientations (CPO) of olivine, pyroxenes, plagioclase and amphibole in a series of samples collected in a profile normal to the shear zone strike. This new data set highlights an evolution, in time and space, of the strain distribution and of the active deformation mechanisms, implying decreasing pressure and temperature conditions, starting under near solidus conditions. Based on these data, we propose a model for the formation and evolution of this mantle shear zone and discuss the constraints these observations place on the processes associated with strain localization in the upper mantle.

2. The Lanzo Massif: Large-Scale Structures

2.1. Geological Context

[5] The Lanzo massif is a 150 km^2 body of relatively fresh plagioclase peridotite located in the western Alps. It is bounded by the Po plain sediments to the East and South, high-pressure metaophiolites and "schistes lustrés" to the West, and continental units of the Sesia zone in the North (Figure 1). The peridotites are enveloped in a thick serpentinite belt (≤6 km), which resulted from both ocean floor alteration and Alpine metamorphism [*Pelletier and Müntener*, 2006]. They form the basement of an oceanic sequence considered to be a part of the Piemont-Ligurian oceanic plate [*Lagabrielle et al.*, 1990; *Pelletier and Müntener*, 2006; *Kaczmarek et al.*, 2008] that was subducted up to eclogite facies before fast exhumation during the Alpine orogenesis [*Compagnoni and Sandrone*, 1979; *Kienast and Pognante*, 1988; *Pelletier and Müntener*, 2006]. Pervasive eclogitic metamorphic equilibration is however restricted to the borders of the Lanzo massif [*Kienast and Pognante*, 1988].

[6] The massif is composed by three peridotite bodies (the northern, the central, and the southern

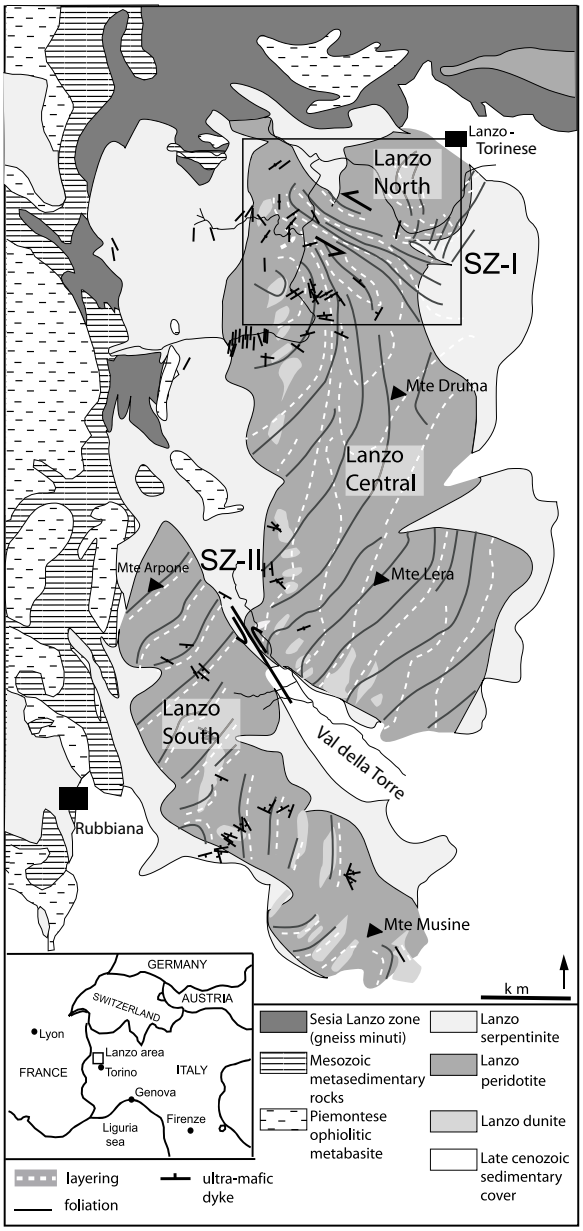

Figure 1. Geological map of the Lanzo massif (modified from *Boudier* [1978]). The box represents the studied area.

bodies) separated by two NW-SE striking shear zones (Figure 1) [*Boudier*, 1972; *Boudier and Nicolas*, 1972; *Boudier*, 1978; *Kaczmarek and Müntener*, 2008]. The northern body is traditionally interpreted as a piece of ancient subcontinental lithospheric mantle composed of depleted material, which was separated from the convective mantle and accreted to subcontinental lithosphere >400 Ma years ago [*Bodinier et al.*, 1991; *Piccardo et al.*, 2007b]. The southern body was proposed to have formed as a high-temperature asthenospheric mantle diapir, which rose from the garnet stability field to shallow depths, being submitted to a large degree of melt extraction [*Nicolas*, 1968; *Bodinier et al.*, 1991]. The central body displays transitional geochemical features [*Bodinier et al.*, 1991]. *Müntener and Piccardo* [2003] proposed that it represents a subcontinental lithospheric mantle modified by thermochemical erosion in an extensional, preoceanic setting. Widespread interaction with mid-ocean ridge basaltic (MORB-type) melts is recorded in the Lanzo massif by formation of pyroxene-depleted reactive spinel peridotites, plagioclase-enriched impregnated peridotites, and replacive spinel harzburgite-dunite channels; all lithologies were later intruded by MORB-type gabbroic dykes [*Boudier*, 1972; *Bodinier et al.*, 1991; *Müntener and Piccardo*, 2003; *Piccardo et al.*, 2007a; *Kaczmarek and Müntener*, 2010].

[7] The entire peridotite massif displays a pervasive high-temperature foliation and lineation, defined by alignment of spinel aggregates, plagioclase-rich lenses, and elongation of pyroxene porphyroclasts, and a cm-scale compositional layering marked by variations in pyroxene content. The orientation of this foliation varies across the massif, rotating from N-S and NE-SW strike in the southern and central domains, to NW-SE strike in the shear zone area and N-S in the northern domain (Figure 1); the lineation is generally subhorizontal. The pyroxenite layering and the foliation are discordant in the central and northern bodies, but they are concordant in the southern body and within the northern shear zone (Figures 1 and 2). The high-temperature foliation of the central body gradually rotates into parallelism with the northern shear zone (SZ-I) over a distance of 2–3 km (Figure 2). A much sharper foliation rotation is observed at the northern limit of the shear zone. Analysis of the reorientation of the high-temperature foliation and lineation as it enters the northern shear zone suggests a sinistral displacement across it (Figure 1). In contrast, in the strongly serpentinized southern shear zone (SZ-II), the foliation reorientation takes place over a much shorter length scale (Figure 1). These observations suggest lower-temperature conditions for the formation of the SZ-II relatively to SZ-I.

2.2. The Northern Lanzo Shear Zone

[8] Five deformation textures are asymmetrically distributed along a transect normal to the northern shear zone (SZ-I) strike (Figure 2). From southwest to northeast, grain sizes gradually decrease from the coarse porphyroclastic to the mylonitic peridotites.

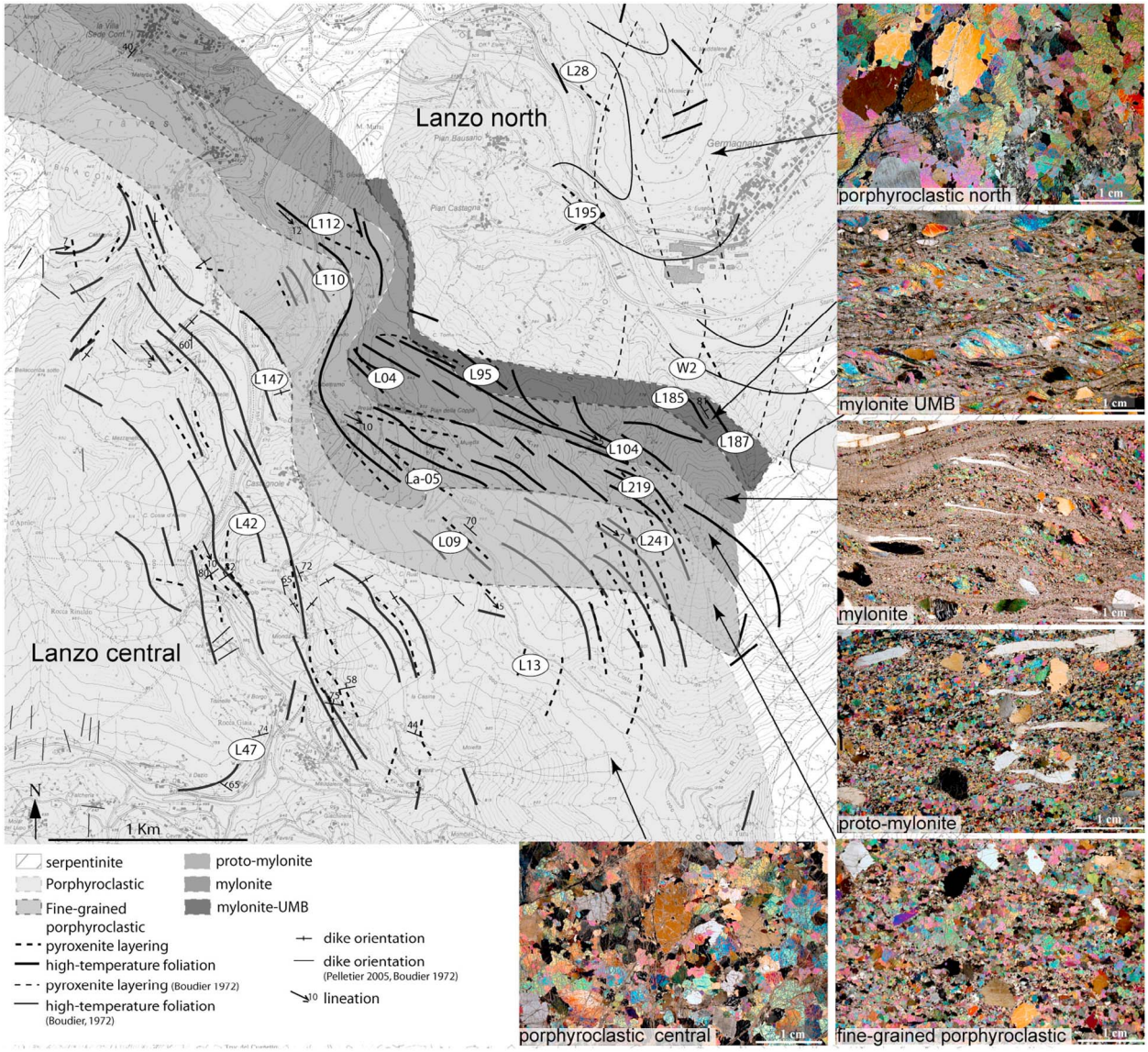

Figure 2. Structural map of the northern Lanzo shear zone (modified from *Kaczmarek and Müntener* [2008]), showing the distribution of deformation microstructures (illustrated by cross-polarized light microphotographs on the right), the orientation of the foliation and of the pyroxenite layering, as well as the location of the analyzed samples. UMB, ultramylonite bands.

In contrast, the northeastern limit of the shear zone is characterized by a sharp transition, over <100 m, from mylonites with ultramylonite bands (UMB) to coarse porphyroclastic peridotites (Figure 2).

[9] This variation in deformation textures is accompanied by a change in the major and trace elements contents of the peridotites. Increasing deformation from porphyroclastic to mylonitic peridotites is associated with more homogeneous compositions (Al_2O_3, TiO_2, Na_2O, NiO, Yb, Sm) and a general tendency for enrichment in basaltic components [*Kaczmarek and Müntener*, 2010]. The evolution of trace element contents of the peridotites within the studied area is reproduced by refertilization models where an E-MORB produced by melting of a spinel-peridotite percolates a depleted peridotite [*Kaczmarek and Müntener*, 2010]. Rare earth elements (REE) contents also indicate a less enriched composition of the northern body relative to the central body.

[10] Microstructural evidence for widespread melt-rock reaction includes (1) crystallization of interstitial, mostly exsolution-free orthopyroxene along olivine-olivine grain boundaries or across olivine porphyroclasts and (2) crystallization of orthopyroxene + plagioclase at the expense of clinopyroxene [*Kaczmarek and Müntener*, 2008]. These

microstructures are well preserved in the coarse-grained peridotites or within large porphyroclasts in the protomylonitic or mylonitic peridotites. They tend to be obliterated in fine-grained mylonites, indicating that deformation continued under subsolidus conditions.

[11] Gabbroic and basaltic dykes are common in the central domain, where they crosscut the high-temperature foliation of the peridotites, but never observed north of the shear zone. Centimetric amphibole-bearing gabbro dykes parallel to the foliation are however observed in the mylonites with UMB.

3. Microstructural Evolution Across the Northern Lanzo Shear Zone

[12] At the thin section scale, the coarse porphyroclastic texture is characterized by a more continuous grain size distribution than the other textures (Figure 2). Porphyroclasts of olivine, orthopyroxene, and clinopyroxene up to 1 cm wide are associated with smaller crystals of olivine, orthopyroxene, clinopyroxene, plagioclase, and spinel. These smaller crystals have an average grain size of 0.5 to 1.5 mm (this estimation is poorly constrained due to the high grain size variability) and a weak shape preferred orientation (SPO). Olivine porphyroclasts have irregular shapes with a weak elongation (aspect ratios are usually less than 1:3) marking the lineation. Subgrain boundaries perpendicular to the grain elongation are common. Orthopyroxene porphyroclasts have rounded or irregular shapes with a weak elongation parallel or at low angle to the olivine lineation. They display numerous thin clinopyroxene exsolutions. Clinopyroxenes with thin orthopyroxene exsolutions are usually finer grained (~0.5 mm). Plagioclase occurs both as coronas around spinel and as an independent phase, usually with interstitial shapes. Spinel is distributed randomly in the samples, most often with rounded shapes rimmed by plagioclase. In most samples, vermicular pargasitic Ti hornblende (10–50 μm) rims clinopyroxene; it also occurs as elongated interstitial grains, suggesting postkinematic reaction with melts or fluids at temperatures higher than 1100°C [*Niida and Green*, 1999].

[13] The transition to the fine-grained porphyroclastic texture is characterized by decreasing abundance and average grain size of porphyroclasts (<0.8 mm) and a more bimodal grain size distribution (Figure 2). Recrystallized minerals from the matrix have an average grain size of 0.25 mm and display a weak SPO subparallel to the elongation of the porphyroclasts (Figure 3a). Relative to the coarse porphyroclastic texture, olivine porphyroclasts show more closely spaced subgrain boundaries (Figure 3a). Orthopyroxenes are usually smaller than 1 cm and display numerous thin clinopyroxene exsolutions; they tend to have elongated shapes with aspect ratios up to 5:1, but equiaxed crystals are also observed. Clinopyroxenes are smaller (<0.5 mm) and have thin orthopyroxene exsolutions. Plagioclase is usually interstitial (average grain size ~0.3 mm, Figure 3b) and has twins preferentially oriented parallel to the foliation, indicating some crystal preferred orientation, but randomly oriented plagioclase aggregates forming lenses parallel to the foliation are also observed (Figure 3b). In all cases, it shows well-developed mechanical twins (Figure 3b). Spinels are usually 0.5 to 1 mm long; they have irregular shapes, but align parallel to the lineation. The foliation and lineation are thus defined by spinels alignment and the SPO of orthopyroxene and olivine. As in the porphyroclastic texture, Ti hornblende often rims clinopyroxene.

[14] The protomylonitic texture is characterized by further grain size reduction of both porphyroclasts (~1 mm in size) and recrystallized minerals in the matrix (100 to 450 μm) (Figures 2, 3c, and 3d). The matrix proportion generally exceeds 25%–30%; it is composed of olivine, pyroxenes, spinel, and plagioclase and forms an anastomosed network enclosing the porphyroclasts. The foliation is thus underlined by the shape-preferred orientation of the porphyroclasts and the orientation of the fine-grained bands. Aligned spinels and highly elongated orthopyroxene porphyroclasts (aspect ratios may reach 10:1) with strong undulose extinction and numerous thin exsolutions mark the lineation (Figure 3c). Crystals in the matrix also display a weak SPO parallel to the porphyroclasts one and intracrystalline deformation features as undulose extinction (Figure 3c). Olivine porphyroclasts are almost entirely recrystallized and form lenticular aggregates with a slightly coarser grain size than the matrix (Figure 3c). Clinopyroxenes occur either as small porphyroclasts (<1 mm) or dispersed in the matrix; they usually display orthopyroxene exsolutions. Plagioclase occurs associated with spinel, dispersed in the matrix, or forming lenses (Figure 3d); in the latter crystals have irregular shapes, but are usually elongated parallel to the foliation and show deformation twins. Ti hornblende rims clinopyroxene.

[15] The mylonitic texture is characterized by extremely stretched orthopyroxene porphyroclasts (aspect ratios up to 20:1), relatively coarse grained

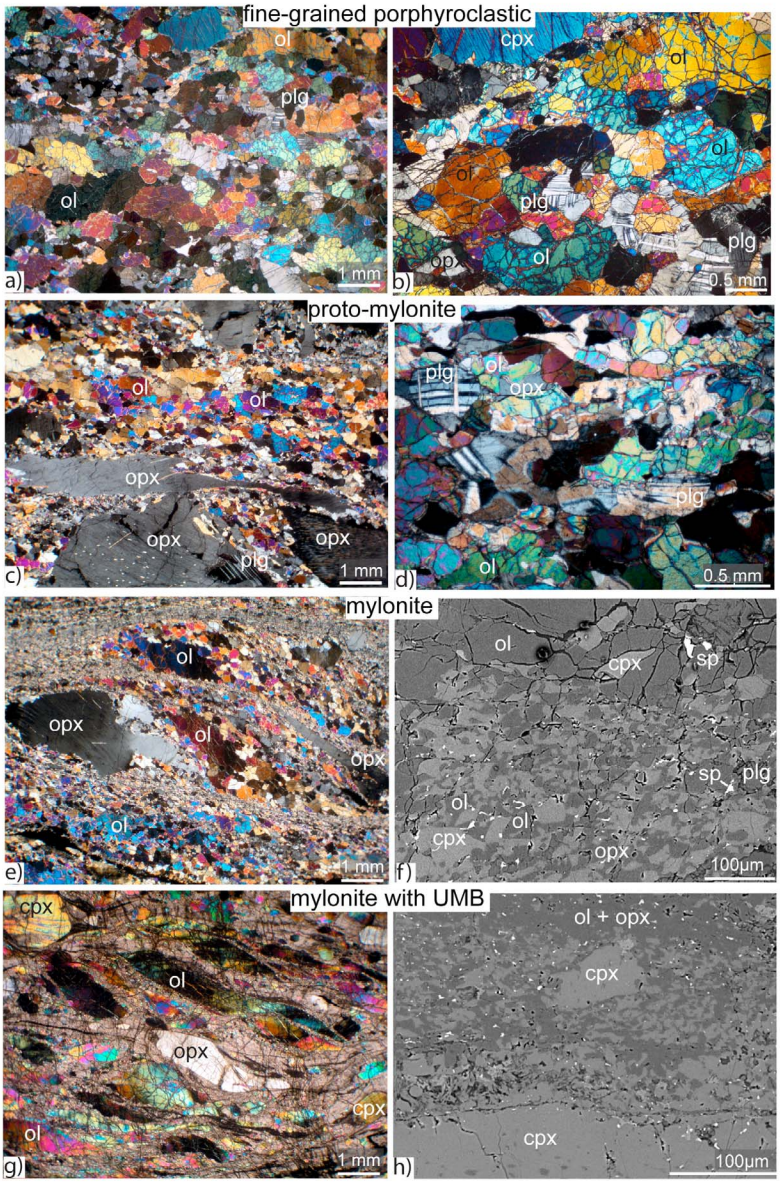

Figure 3. Photomicrographs and backscattered electron (BSE) images of peridotites displaying characteristic features of the different deformation facies at (a, c, e, g) small and (b, d, f, h) large enhancements. Figure 3a shows fine-grained porphyroclastic texture. Figure 3b shows fine-grained porphyroclastic matrix with a weak preferred orientation of the recrystallized minerals parallel to the foliation. Figure 3c shows protomylonitic texture. Figure 3d shows protomylonite matrix displaying a SPO of the crystals and deformed and elongated plagioclases parallel to the foliation. Figure 3e shows mylonitic texture with elongated orthopyroxene porphyroclasts. Figure 3f is a BSE image of the fine-grained matrix in amylonite composed of olivine, pyroxenes, spinel, and plagioclase. Figure 3g shows mylonite with ultramylonite bands. Figure 3h is a BSE image of an ultramylonite band illustrating the heterogeneous distribution of mineral phases. It displays domains enriched in orthopyroxene + olivine or olivine + clinopyroxene + amphibole, ±orthopyroxnene. Abbreviations are as follows: ol, olivine; opx, orthopyroxene; cpx, clinopyroxene; plg, plagioclase; sp, spinel.

olivine-rich lenses, and a fine-grained matrix that forms an anastomosed network of mm-wide fine-grained bands underlining the foliation (Figures 2 and 3e). Orthopyroxene porphyroclasts have an undulose extinction and contain numerous thin exsolutions. Olivine-rich lenses are essentially composed of relict porphyroclasts with a high density of subgrains surrounded by recrystallized grains with a coarser texture (50–250 μm, Figure 3e). Exsolved clinopyroxenes are almost fully recrystallized (aver-

age recrystallized grain size is 150 μm), forming elongated lenses in the foliation plane (Figure 4a). Spinel occurs scattered in the matrix; it has irregular, but elongated shapes, marking the lineation. Plagioclase occurs as aggregates surrounding coarse spinels (<2 mm), in polycrystalline lenses elongated parallel to the lineation, or as isolated crystals; the latter have irregular shapes, but are usually flattened in the foliation (Figure 3e). The fine-grained matrix (5–50 μm) is composed by intermixed olivine, orthopyroxene and clinopyroxene, spinel, plagioclase and Ti hornblende (Figure 3f). The phase distribution is however heterogeneous; it alternates domains composed of intermixed olivine + clinopyroxene + plagioclase or olivine + orthopyroxene (symplectite-like microstructure, Figure 4b). All phases have irregular shapes with interpenetrating grain boundaries, but olivine and, sometimes, pyroxenes tend to display a weak SPO at low angle to the band trend (Figures 3f and 4b). Plagioclase in the matrix is usually dispersed, but it locally forms aggregates with coarser grain sizes than other matrix phases. It displays undulose extinction and deformation twins. Recrystallized clinopyroxenes are usually rimmed by amphibole (Ti hornblende), but the latter also occurs dispersed in the fine-grained matrix within clinopyroxene-rich domains. A characteristic feature of these mm-scale fine-grained bands is the development of planar interphase grain boundaries aligned parallel to the band trend (Figure 3f). In contrast, the limits of the fine-grained bands with porphyroclasts or coarse-grained lenses are irregular (Figure 3f).

[16] The mylonite with ultramylonite bands (UMB) is characterized by a more heterogeneous grain size distribution, where a penetrative anastomosed network of mm-wide ultramylonitic bands encloses large lens-shaped olivine and pyroxene porphyroclasts or coarse-grained domains (Figures 2 and 3g). Olivine and pyroxenes porphyroclasts are coarser (up to 8 mm long) and less recrystallized than those in mylonite and protomylonite textures. They are highly asymmetric, consistently indicating sinistral shearing (Figure 3g). Olivine porphyroclasts display closely spaced subgrain boundaries and strong undulose extinction suggesting deformation at high-stress, low-temperature conditions. They are often surrounded by aggregates of recrystallized olivine with coarser grain sizes (50–250 μm) and roughly polygonal shapes. Exsolved orthopyroxene and clinopyroxene porphyroclasts are strongly stretched, being sometimes fragmented into several pieces; they underline the lineation (Figures 2 and 3g). Pyroxene porphyroclasts have irregular limits, being usually surrounded by a polymineralic corona with composition similar to the neighboring ultramylonitic matrix, but with coarser grain size (Figure 3h). The UMB are very similar to the mm-scale fine-grained bands observed in the mylonites, but grain sizes are still smaller (5 to 30 μm, Figure 3h). They are composed by olivine, pyroxenes, plagioclase (completely altered), spinel, and Ti hornblende. As in fine-grained bands in the mylonites, these phases are heterogeneously distributed in the matrix, which contains domains enriched in a particular mineral assemblage (e.g., the clinopyroxene + Ti hornblende + olivine domain in Figure 4d). All phases have irregular shapes and interpenetrating grain boundaries (Figures 3h, 4d, and 6e). Surprisingly, planar grain boundaries subparallel to the band trend are less developed than in fine-grained bands in the mylonites (Figure 3h). Orthopyroxene and clinopyroxene in UMB display more equiaxed shapes than olivine, but a weak SPO subparallel to the band trend is observed for all phases (Figures 3h and 4d). Spinels are elongated and underline the lineation. Amphibole (Ti hornblende) is more abundant in the UMB than outside and it partially replaces clinopyroxene neoblasts (Figure 4d).

4. Crystallographic Preferred Orientation Data

4.1. Sampling and Method

[17] To further characterize the evolution of the deformation in the Lanzo shear zone, we analyzed the crystal preferred orientations (CPO) of olivine, orthopyroxene and clinopyroxene, as well as plagioclase and amphibole when it was possible, in 16 lherzolites and 2 harzburgites representative of the textural variation across the shear zone. Thin sections were prepared from oriented samples and were cut perpendicular to the foliation and parallel to the lineation (XZ sections). Crystal-preferred orientations (CPO) were measured by indexing of Electron Backscattered Diffraction (EBSD) patterns using the JEOL JSM 5600 SEM-EBSD system at Géosciences Montpellier.

[18] For each sample, we obtained crystallographic orientation maps covering most of the thin section (maps are usually 20*35 mm) with a regular grid step ranging from 35 μm in the mylonites to 60 μm in the coarse porphyroclastic samples (Figures 4a and 4c). High-resolution maps with a 1, 2, or 3 μm grid step were performed in fine-grained bands using the CamScan Crystal Probe X500-FE SEM-EBSD system at Géosciences Montpellier

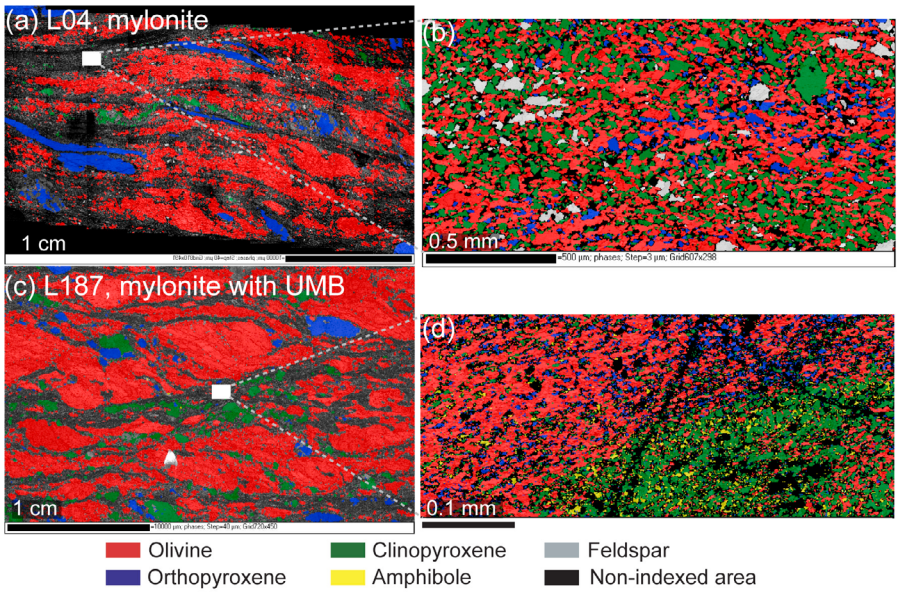

Figure 4. Phase distribution maps derived from the EBSD data for (a) mylonite L04 and (c) mylonite with ultramylonite bands L187. Detailed maps of (b) a fine-grained band in L04 and (d) an ultramylonite band in L187.

(Figures 4b and 4d). Average raw indexation rates are of 65%. Postacquisition data treatment allowed to further increase the indexing rate by (1) filling the nonindexed pixels that have up to 8 identical neighbors with this orientation; (2) repeating this operation using 7, 6, and 5 identical neighbors; (3) identifying the grains, i.e., continuous domains characterized by an internal misorientation <15°; and (4) within each olivine crystal, searching and correcting for systematic indexing errors due to the olivine hexagonal pseudosymmetry, which results in similar diffraction patterns for orientations differing by a rotation of 60° around [100]. At each step the resulting orientation maps were checked to avoid overextrapolation of the data.

[19] In addition to the CPO, EBSD mapping of the entire thin sections also provides information on the modal composition (Figure 4) and microstructure (distribution of the various mineral phases, grain sizes and shapes). These microstructural data were constrained by optical microscopy observations (Figures 2 and 3). Pole figures are represented using average Euler angles for each grain instead of individual measurements to avoid overrepresentation of large grains on thin section. Additionally, we set up a minimum grain area from 8000 μm^2 to 25200 μm^2 (for instance, 8575 μm^2 in a map with a 35 μm step grid) to avoid over-representation of poorly indexed grains. This minimum area is set small enough not to lose information on the orientation of the smaller grains of the section.

4.2. Crystal Preferred Orientation Data

[20] All Lanzo peridotites, except the mm-scale fine-grained bands, have a well-developed olivine CPO, with a preferred orientation of [100] parallel or within <15° of the lineation, and a concentration of [010] axes close to the pole of the foliation (Figure 5). [001] axes are more dispersed but often show a weak maximum in the foliation plane at high angle to the lineation. A closer inspection highlights however variations in the CPO symmetry from sample to sample. Porphyroclastic lherzolite from the northern domain as well as a sample from the porphyroclastic central domain show axial [100] patterns characterized by a strong concentration of [100] at low angle (<10°) to the lineation and a girdle distribution of [010] and [001] normal to it. However, most coarse porphyroclastic lherzolites of the central domain display axial [010] patterns marked by a strong concentration of [010] normal to the foliation and girdle distributions of [100] and [001] at low angle to the foliation. These variations in the symmetry of the olivine CPO are accompanied by similar changes in the orthopyroxene CPO symmetry (see description below).

[21] Fine-grained porphyroclastic samples, protomylonites, and mylonites have weaker, orthorhombic olivine CPO patterns marked by similar concentrations of [100] and [010] parallel to the lineation and normal to the foliation, respectively (Figure 5). The relation between olivine CPO and microstructure is illustrated by crystal orientation

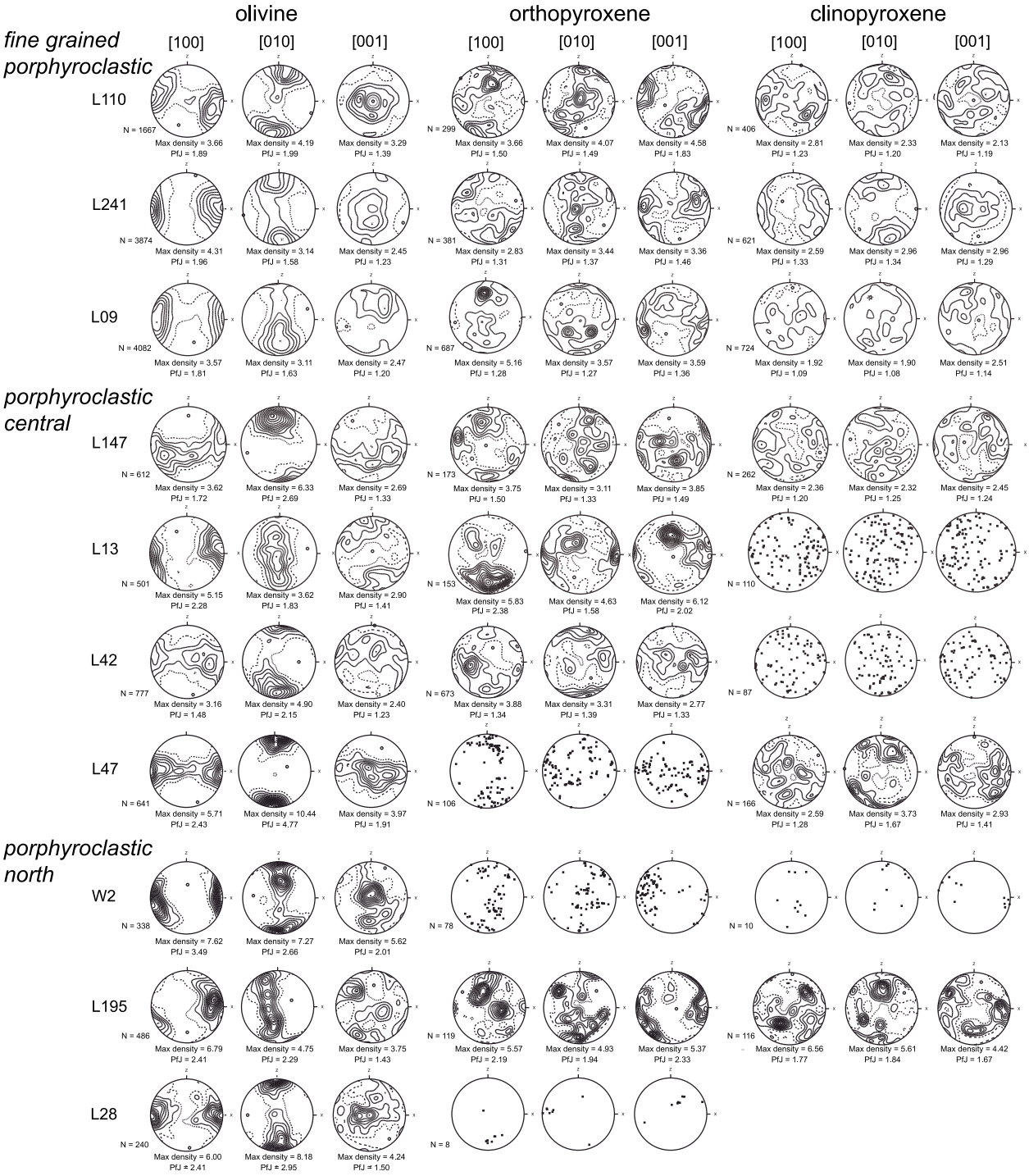

Figure 5. Crystal preferred orientations (CPO) of olivine, orthopyroxene, clinopyroxene, and plagioclase in samples representative of the different microstructures collected along a section normal to the shear zone trend (samples' locations are indicated in Figure 2). Equal-area lower hemisphere stereographic projections in the structural reference frame (X represents the lineation, and Z is the normal to the foliation). Pole figures are plotted using average Euler angles for each grain instead of individual measurements to avoid overrepresentation of larger grains on the thin section; n is the number of measured grains. Contours at 0.5 multiple of uniform distribution intervals. Stereoplots were not contoured when numbers of measured grains is lower than 110. PFJ is a scalar measure of the strength of the axis orientation.

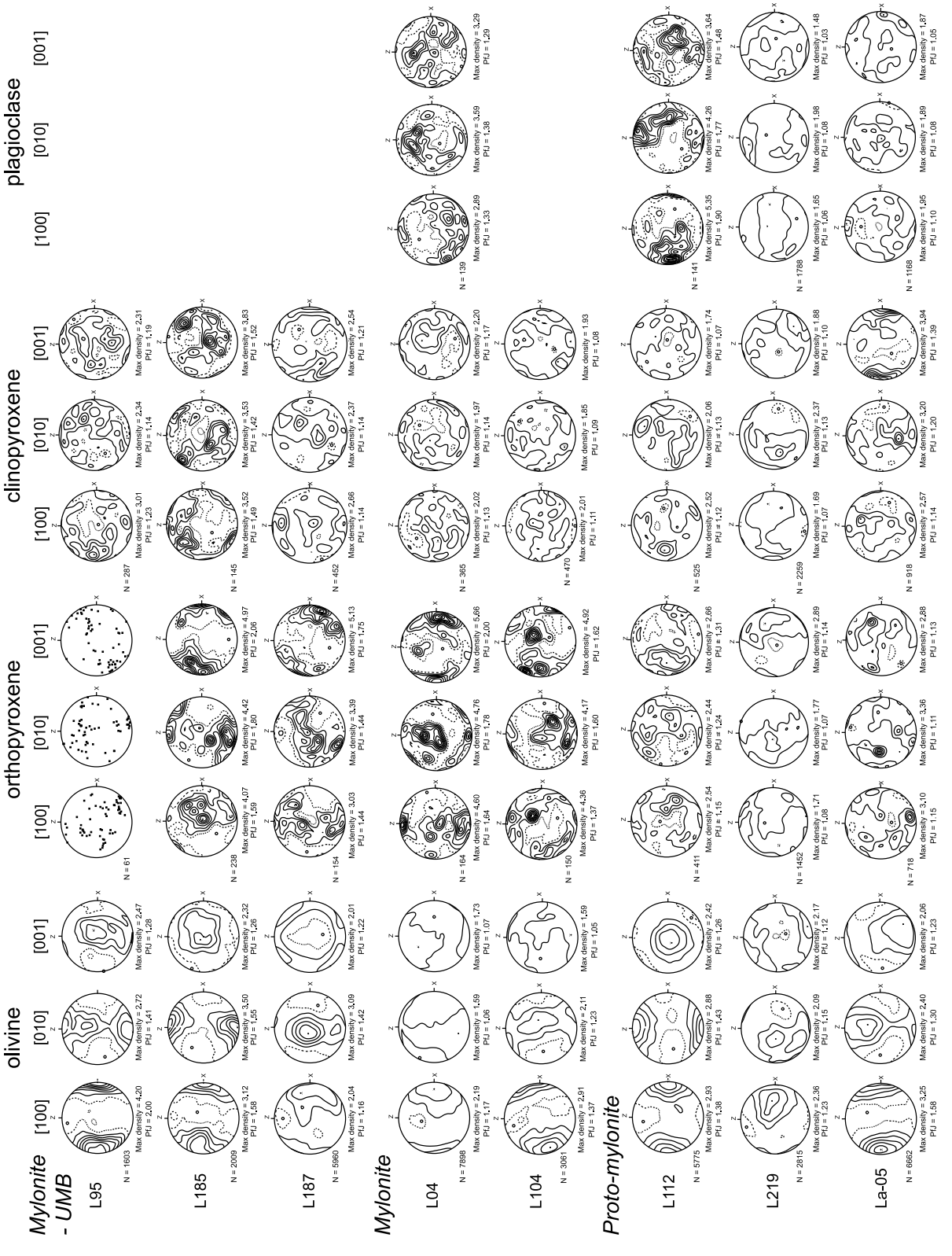

Figure 5. (continued)

maps colored as a function of the orientation of the lineation (X) in the crystal reference frame (Inverse Pole Figure IPF coloring scheme) for a mylonite with UMB, a mylonite, and a protomylonite. Olivine porphyroclasts in the mylonite with UMB sample display a strong orientation of [100] parallel to the lineation (high proportion of blue-colored crystals, Figure 6a). Most porphyroclasts are surrounded by a corona of recrystallized olivine grains, which display more varied orientations with a high proportion of crystals with [001] parallel to the lineation (reddish crystals). In the mylonite and protomylonite samples (Figures 6b and 6c), porphyroclasts are also dominantly bluish colored, indicating a preferred orientation of olivine [100] axes parallel to the lineation, but have a more patchy aspect due to the high density of subgrains and dynamically recrystallized neoblasts. Farther from the porphyroclast cores, recrystallized grains display more varied orientations: many crystals have [U0V] axes subparallel to the lineation (rose and red crystals, Figure 6b), and a few have [010] axes at low angles to the lineation (greenish ones). In the protomylonite, changes in orientation in the recrystallized domains are more gradual (Figure 6c).

[22] CPO strength may be quantified by the J index, which is the volume-averaged integral of the squared orientation densities and hence is sensitive to peaks in the orientation distribution function [*Bunge*, 1982]. J index of the olivine CPO was calculated based on the mean orientation for each grain using SuperJ7x program by D. Mainprice with a 10° Gaussian half-width, data at 1° bins, and truncation of the orientation distribution function (ODF) at degree 22. More than 500 individual orientation measurements were used for all samples, except two coarse porphyroclastic peridotites from the northern domain for which 240 and 338 measurements were used. Even the lowest value is largely superior than the minimum of 100 measurements that was shown necessary to avoid overestimation of the CPO strength [*Lapierre et al.*, 1996]. There is an evident correlation between the microstructure, the position within the shear zone, and the olivine J index (Figure 7). The highest J indexes are observed for coarse porphyroclastic peridotites from the northern part of the Lanzo massif (J > 8) and the lowest J indexes are recorded by mylonitic peridotites and in the fine-grained bands (J < 3). There is also a clear correlation between the olivine J index and the average grain size (Figure 7). Both values decrease progressively across the southern boundary of the shear zone, from the coarse-grained porphyroclastic lherzolites of the central domain of the massif (J = 5–7, average recrystallized grain size = 400 μm) to the mylonites (J < 3, average recrystallized grain size = 150 μm). In contrast, the northern boundary of the shear zone is characterized by a sharp increase in both average olivine grain size and J index (J > 8, average recrystallized grain size >580 μm).

[23] Orthopyroxenes CPO in most samples are well correlated with the olivine CPO (Figure 5). The maximum concentration of olivine [100] axes and of orthopyroxene [001] axes, which are the dominant glide directions for these minerals at high-temperature, low-pressure conditions (see reviews by *Nicolas and Poirier* [1976] and *Tommasi et al.* [2000]) are usually subparallel, displaying a slight obliquity (<10°) to the lineation marked by the crystals elongation. Moreover, in those samples that show axial [010] olivine CPO patterns (samples L47, L147, L42), the orthopyroxene [001] axes are also dispersed in the foliation plane. Orthopyroxene [100] and [010] axes are more dispersed, but either [100] or [010] tend to form a girdle normal to the foliation in most coarse-grained peridotites. Orthopyroxene CPO in the fine-grained porphyroclastic and protomylonitic samples are weak, but still correlated to the olivine CPO. In contrast, orthopyroxenes porphyroclasts and recrystallized grains in the mylonite and mylonite with UMB samples show a well-developed CPO similar to the one recorded in porphyroclastic peridotites. The maximum concentration of the orthopyroxene [001] axis is perfectly correlated, without obliquity, to the olivine [100] axis orientation.

[24] Clinopyroxenes have weak and highly variable CPO patterns, which do not show a clear correlation with the microstructure. In the coarse-grained peridotites, clinopyroxene CPO are mostly uncorrelated to both olivine and orthopyroxene CPO (Figure 5). Lack of correlation between the clinopyroxene and olivine or orthopyroxene CPO also characterizes most fine-grained samples. However, some protomylonites and mylonites with UMB, like samples La-05, L185 and L187, show a good correlation between the clinopyroxene and olivine CPOs, with maximum concentration of the clinopyroxene [001] axes roughly parallel to the concentration of [100] axes of olivine (Figure 5).

[25] Plagioclase CPO was measured in 1 mylonitic and 3 protomylonitic samples (Figure 5); the remaining samples have low modal contents of plagioclase and the number of crystals measured was not enough to define a significant CPO. Except for the protomylonite L112, where the [100] and [010] axes

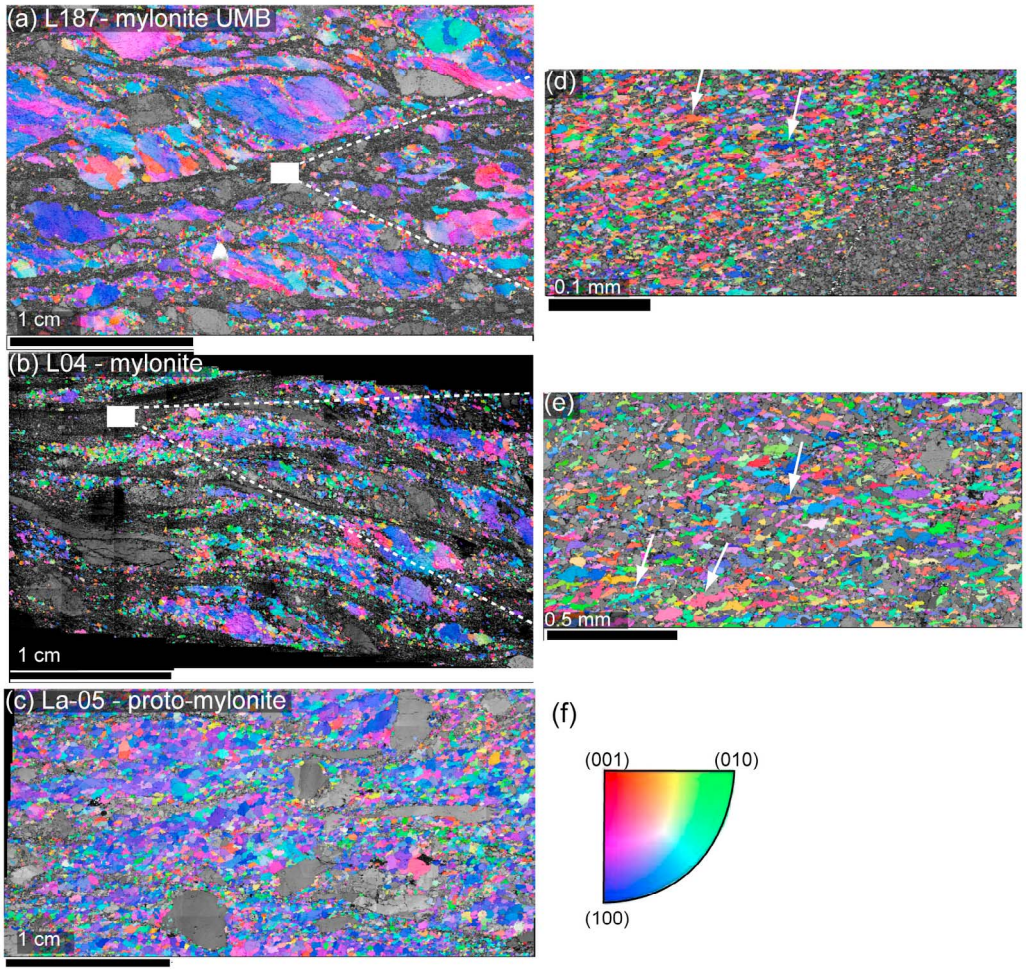

Figure 6. CPO maps for olivine: (a) mylonite with ultramylonite bands L187. (b) mylonite L04. and (c) protomylonite La-05. Detailed maps of (d) an ultramylonite band in L187 and (e) a fine-grained band in L04. Coloring as a function of the orientation of the lineation in the crystal reference frame as indicated in (f) the inverse pole figure (see text for detailed description). White arrows indicate elongated olivine crystals in the fine-grained and ultramylonite bands.

form clear point concentrations at low angle to the lineation and normal to the foliation, respectively, plagioclase CPO is very weak. Protomylonites L219 and La-05 show nevertheless a wide girdle of [100] parallel to the foliation and a preferred orientation of [010] normal to it. In the mylonite L04, the plagioclase CPO is very dispersed and does not show a clear correlation with the other phases' CPO.

4.3. CPO in mm-Scale Fine-Grained and Ultramylonitic Bands

[26] In mm-scale fine-grained bands within mylonites and in mm-scale ultramylonitic bands, all minerals display very weak, almost random CPO (Figure 8). In all samples except L104 a weak concentration of olivine [100] axes parallel to the band trend and to the lineation outside the band is nevertheless observed. Olivine [010] axes also tend to form a weak concentration normal to the band orientation or a wide girdle normal to the lineation. The higher dispersion of the olivine CPO in fine-grained bands relatively to the coarse-grained domains is clearly visible in crystal orientation maps colored as a function of the orientation of the lineation (X0) in the crystal reference frame (Figure 6). Olivines in the fine-grained bands display varied colors, indicating highly dispersed orientations, but with a slight predominance of crystals with [100] or [001] parallel to the lineation (higher proportion of bluish to reddish crystals). Analysis of the CPO maps also indicate a slight elongation of the olivine crystals (white arrows on Figures 6d and 6e), which is better developed in

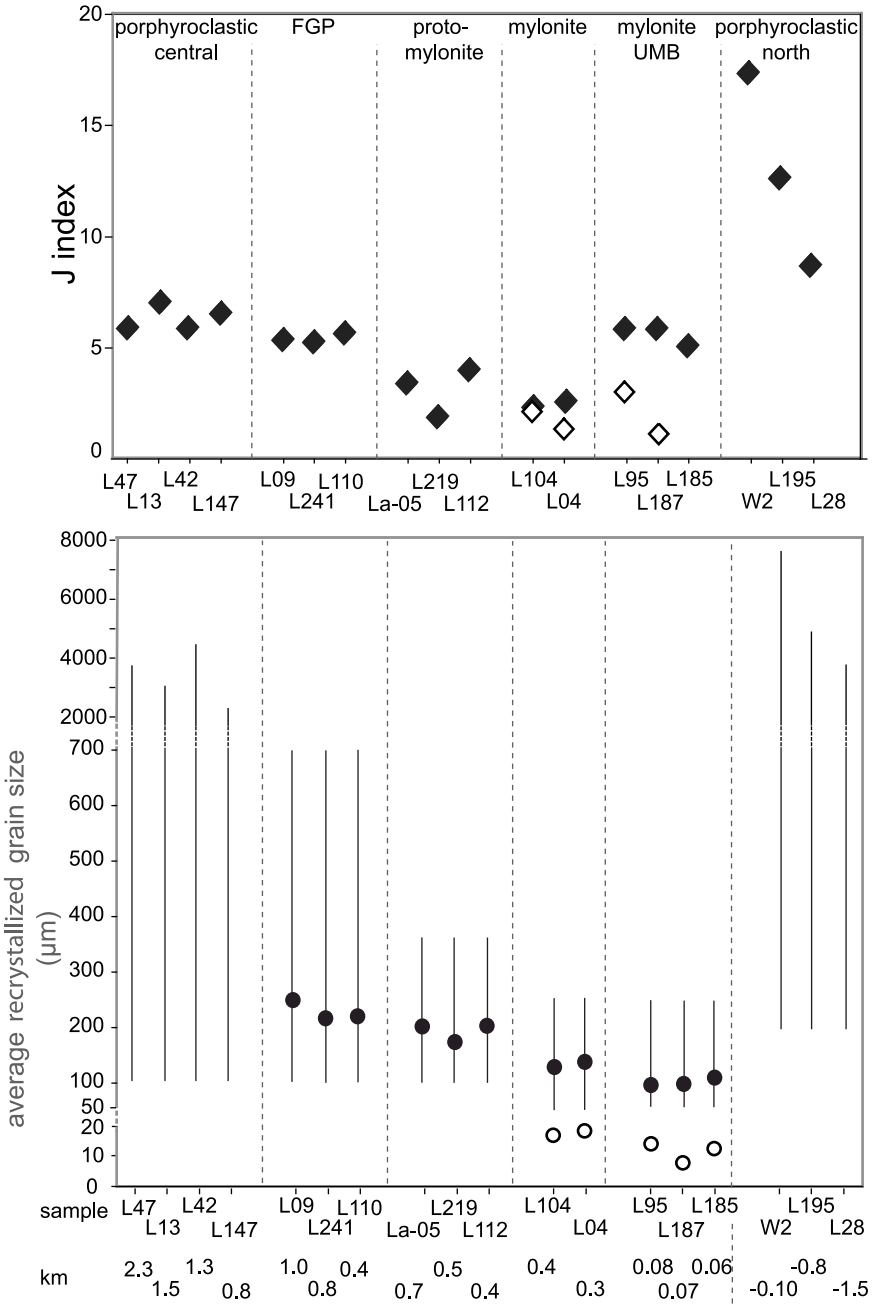

Figure 7. CPO strength characterized by the J index and range of recrystallized grain sizes (diameter in μm) of olivine as a function of the deformation facies and of the distance to the northern limit of the shear zone, defined as the transition between the mylonite with ultramylonite bands and the coarse-porphyroclastic peridotites of the northern domain. In the mylonites, J indexes and recrystallized grain sizes calculated from CPO data for the bulk sample are indicated by solid symbols, and those for the fine-grained and ultramylonite bands are marked by open symbols. For porphyroclastic peridotites, we present the entire range of olivine grain sizes in each sample because in absence of a bimodal grain distribution the discrimination of porphyroclasts and recrystallized grains is impossible. Note the change of the grain size scale between 700 and 2000 μm.

crystals with [100] or [001] axes parallel to the lineation (bluish to reddish colored crystals). This elongation is subparallel to the band trend. In Figure 7, the J index of olivine in the fine-grained and ultramylonite bands in the 5 studied mylonites and ultramylonites is plotted with open symbols. These data shows that these bands have extremely weak olivine CPO ($J < 3$), significantly more dispersed than the olivine CPO in the adjacent coarser-grained domains.

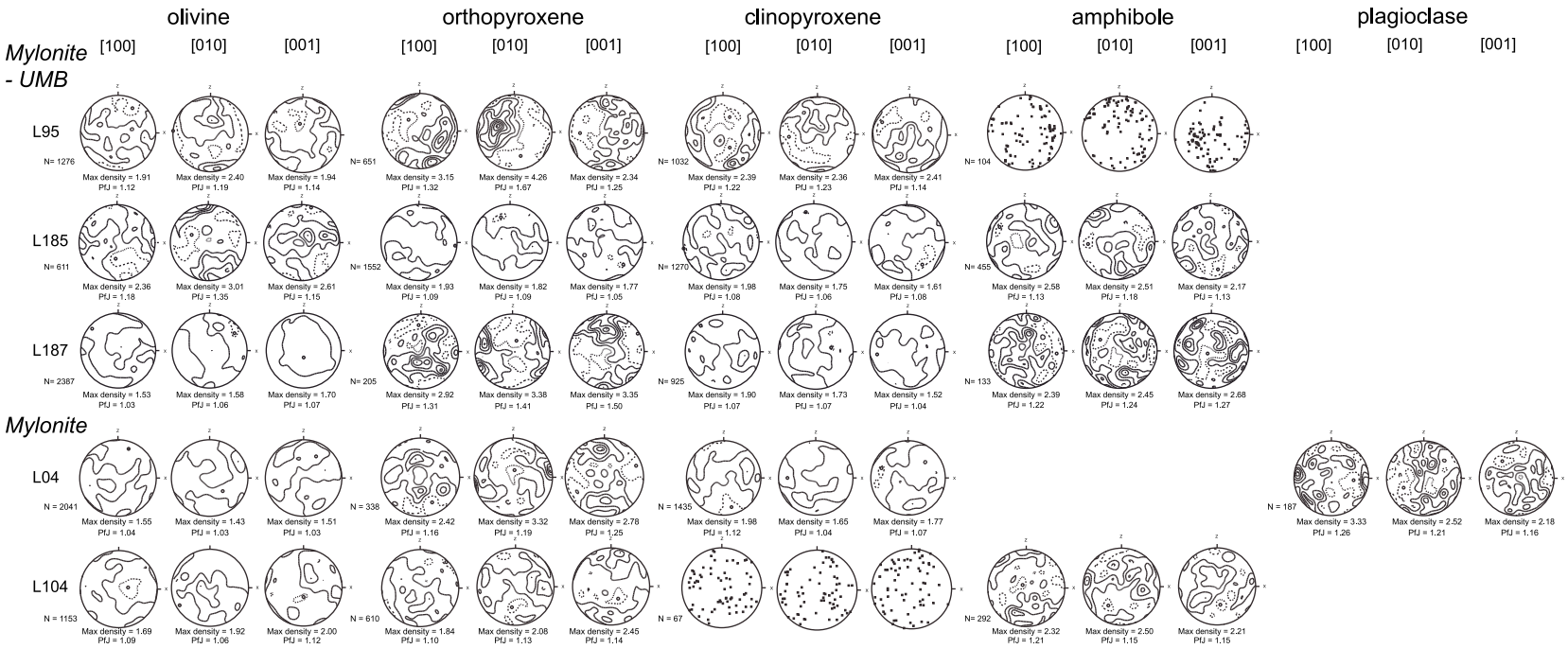

Figure 8. CPO of olivine, orthopyroxene, clinopyroxene, and plagioclase within fine-grained and ultramylonitic bands in mylonites. Equal-area lower hemisphere stereographic projections in the structural reference frame (X represents the lineation, and Z is the normal to the foliation). Pole figures are plotted using average Euler angles for each grain instead of individual measurements to avoid overrepresentation of larger grains on the thin section; N is the number of measured grains. Contours at 0.5 multiple of uniform distribution intervals. Samples were not contoured when numbers of grain is lower than 110.

[27] Orthopyroxene CPO in the fine-grained bands is extremely weak, but it is characterized nevertheless by a weak organization of [001] either as a girdle at high angle to the lineation or in a weak maximum normal to the foliation and a weak concentration of [010] parallel to the lineation (Figure 8). Orthopyroxene CPO is unusually correlated to the olivine CPO: orthopyroxene [010] and [001] axes are subparallel to olivine [100] and [010] axes, respectively.

[28] Clinopyroxenes and amphiboles also display very weak CPO, which are intercorrelated, but not consistent with the orthopyroxene or the olivine CPOs (Figure 8). Plagioclase in the fine-grained bands of mylonite L04 has a weak CPO, which is nevertheless consistent with the olivine one.

4.4. Misorientation Data

[29] Dislocation creep is expected to produce not only distinct crystallographic preferred orientations, but also characteristic misorientation relations, which may be described as the rotation (angle and axis) of the crystal lattice of one grain with respect to its neighbor [*Randle*, 1992; *Wheeler et al.*, 2001]. Dynamic recrystallization by subgrain rotation involves the presence of numerous low-angle or subgrains boundaries within the crystals, resulting in predominance of small rotation angle (<15°) in the correlated (between neighboring measure points) olivine misorientation histograms. Coarse-grained porphyroclastic peridotites and mylonites with UMB display indeed a high frequency of correlated misorientations ≤10°, indicating a high frequency of subgrains (Figures 9a, 9b, and 9f). In fine-grained porphyroclastic peridotites, protomylonites, and mylonites, the predominance of low-angle correlated misorientations is weaker, consistently with the lower proportion of porphyroclasts (Figures 9c–9e). Finally, olivine misorientations in fine-grained bands only differ from the theoretical distribution for a random aggregate by a weak predominance of correlated misorientations <30° (Figures 9g and 9h). This, together with the weak grain elongation, points to a contribution of dislocation creep to deformation even in these fine-grained bands.

[30] Analysis of the misorientation of crystal lattices across low-angle boundaries highlights that, for olivine, rotation axes are mainly normal to [100], with a strong maximum parallel to [010] and a weaker one parallel to [001] (Figure 10). The intensities of these maxima vary from sample to sample and clearly decrease in the fine-grained bands. For orthopyroxene rotation axes accommodating low-angle misorientations concentrate close to [010], consistent with dominant activation of the [001](100) slip system. In the fine-grained bands, rotation axes accommodating low-angle misorientation for both minerals are similar, but more dispersed (Figure 10b).

5. Discussion

5.1. Evolution of the Deformation

[31] The asymmetric distribution of deformation microstructures across the northern Lanzo shear zone (Figure 2) is consistent with progressive strain localization from SW to NE due to deformation under increasing mechanical work rate conditions [*Austin and Evans*, 2007]. Early deformation under high-temperature conditions is recorded in the southern part of the shear zone, while the northern limit records the latest low-temperature deformation steps. Existence of a spatial and temporal gradient in synkinematic temperature conditions is also corroborated by the reorientation of the foliations as one enters the shear zone (Figures 1 and 2). Progressive rotation of the foliation of the coarse-grained peridotites of the central domain into parallelism with the shear zone is consistent with reworking under high-temperature conditions. In contrast, the sharp reorientation of the foliation at the northern limit of shear zone and fast transition from mylonites with UMB to coarse porphyroclastic peridotites (<100 m) suggests deformation under low-temperature conditions. Cooling is also inferred from thermobarometry. Cores and rims of coarse pyroxenes equilibrated at temperatures of 1100–1030°C and 900–840°C at pressures of 1 GPa, respectively, whereas neoblasts in the mylonites and in the ultramylonite bands record still lower equilibrium temperatures of 860–800°C at pressures of 0.5 GPa [*Kaczmarek and Müntener*, 2008].

[32] Early deformation under high-temperature conditions is also suggested by the preservation of microstructures recording synkinematic to late kinematic reactive melt percolation, such as weakly deformed interstitial plagioclase in the coarse porphyroclastic peridotites in the southern part of the shear zone. These microstructures are overprinted by solid-state deformation in the other deformation facies, suggesting lower-temperature, subsolidus conditions during most of the shear zone evolution. The solid-state deformation overprint increases in intensity from the fine-grained porphyroclastic peridotites, where only mechanical twins are observed

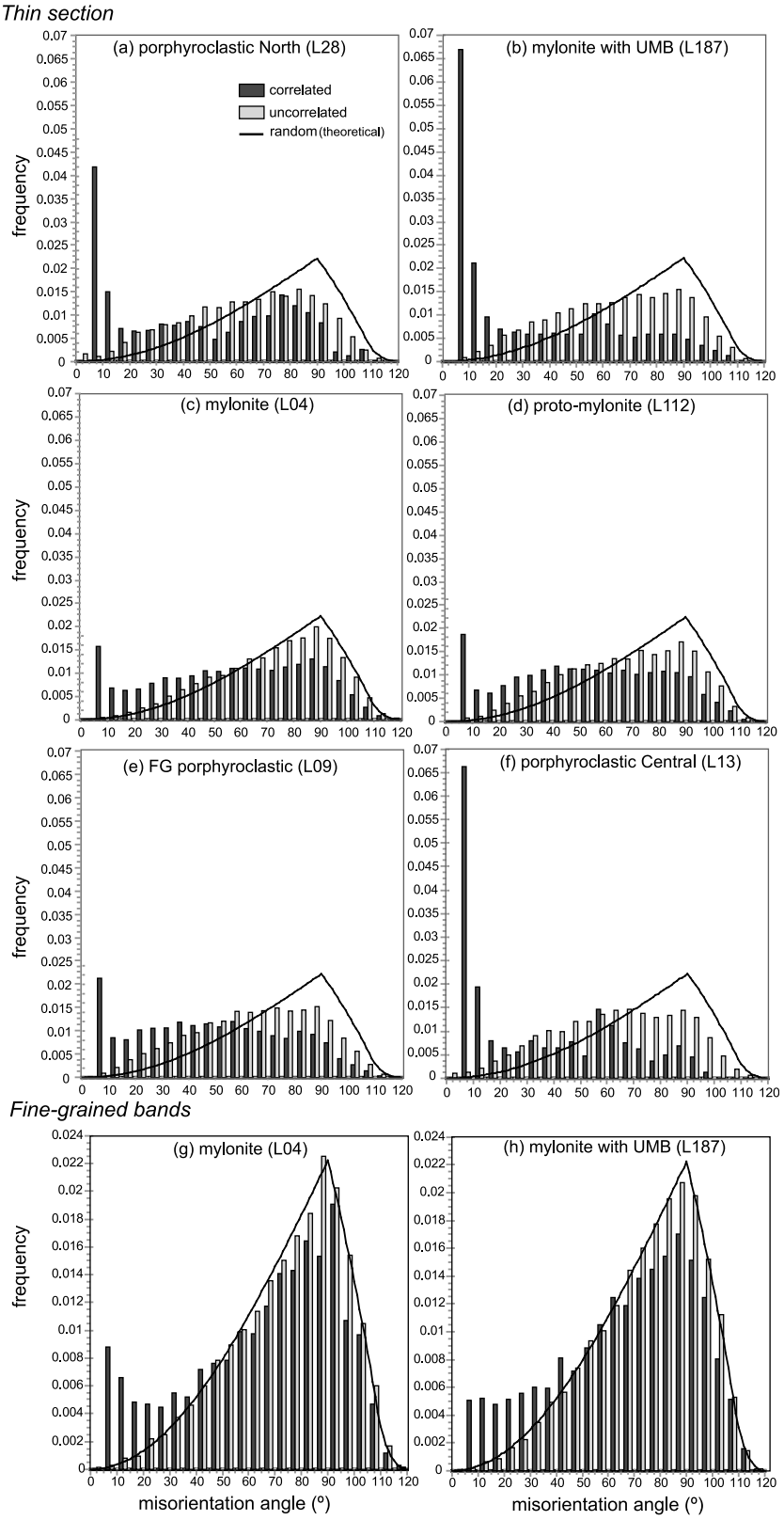

Figure 9. Misorientation angles distribution for olivine in samples representative of the different deformation facies. Correlated misorientations (black) are measured between neighboring points, uncorrelated misorientations (light grey) are measured between randomly selected points, and random indicates the theoretical distribution for a random crystallographic orientation.

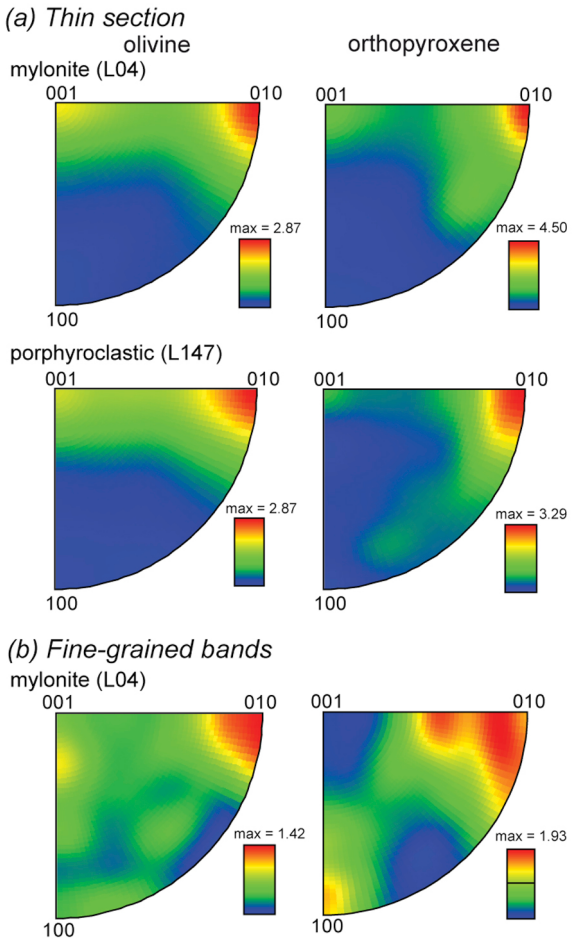

Figure 10. Inverse pole figures of the rotation axes accommodating low-angle misorientations (within grains and across subgrain boundaries) in the crystal reference frame for olivine and orthopyroxene in (a) a porphyroclastic peridotite and a mylonite and (b) an ultramylonitic band in the same mylonite.

(Figure 3b), to the protomylonites and mylonites that show elongated plagioclases with strong undulose extinction and deformation twins (Figures 3c–3e). Moreover, in the porphyroclastic peridotites clinopyroxene and plagioclase CPOs are weak and usually not consistent with the olivine and orthopyroxene CPOs (Figure 5), suggesting some postkinematic crystallization due to melt-rock interaction. CPOs of all phases are however correlated in most protomylonites and mylonites, indicating that deformation continued in the plagioclase stability field under subsolidus conditions (Figure 5). Deformation in presence of melt may also explain the weaker olivine CPO in the coarse-porphyroclastic peridotites of the southern part of the shear zone relatively to those from the northern Lanzo block (Figure 7), since even low melt fractions result in fast diffusion paths, allowing for partial accommodation of the deformation by diffusional processes [*Hirth and Kohlstedt*, 1995a, 1995b]. A decrease in olivine CPO intensity from the least to the most extensively refertilized domains has been indeed observed in the Lherz peridotite massif [*Le Roux et al.*, 2008].

[33] The latest deformation stages, recorded in the mm-scale UMB that characterize the northeastern limit of the shear zone, are accompanied by extensive solid-state reactions, which resulted in development of alternate domains composed by intermixed two- or three-phase assemblages with interpenetrating grain boundaries (symplectite-like microstructure). Similar microstructures have been previously described in a 20–40 m wide ultramylonite band in the Turon de Tecouère peridotite massif in the French Pyrenees and interpreted as the product of a syntectonic continuous net transfer solid-state reaction associated to the spinel to plagioclase-lherzolite transition [*Newman et al.*, 1999].

[34] The northern Lanzo shear zone represents therefore a choice target to investigate the microscopic-scale processes accommodating shearing in the shallow mantle (within the plagioclase-lherzolite stability field, that is above 40 km depth) within an extensional setting. Relatively to mantle shear zones mapped in other peridotite massifs (cf. review by *Dijkstra et al.* [2004]), the northern Lanzo shear zone has two advantages: (1) it records the evolution of deformation under a large range of continuously varying temperature conditions, from near-solidus conditions representative of the lithosphere-asthenosphere boundary to fully lithospheric temperatures (800–900°) and (2) the massif is large enough allowing the exposure of the entire shear zone and of the protoliths on both sides of it.

5.2. Deformation Mechanisms Accommodating Shearing at Different Structural Levels in the Mantle

[35] In spite of grain size decrease by almost two orders of magnitude (from a few mm to tens of μm), all deformation facies (Figures 2, 3, and 5) are characterized by microstructures and crystal preferred orientations typical of deformation dominantly by dislocation creep. Olivine and pyroxenes porphyroclasts and recrystallized crystals display clear SPOs and intracrystalline deformation features, such as strong undulose extinction and subgrains (Figures 2 and 3). Closer spacing of subgrain boundaries in olivine as well as stronger undulose extinction in both olivine and pyroxenes porphyroclasts imply an increase in intracrystalline dislocation densities from the coarse-porphyroclastic

peridotites to the mylonites. Ubiquitous observation of interpenetrating olivine-olivine grain boundaries indicates active grain boundary migration, but length scales of interpenetrations decrease from the porphyroclastic peridotites (Figure 3b) to the mylonites (Figure 3e). These observations together with the decrease of recrystallized grain sizes are consistent with less effective diffusional processes and, hence, deformation under decreasing temperature conditions from the coarse porphyroclastic peridotites to the mylonites. Similarity in subgrain boundary spacing and recrystallized grain sizes in the porphyroclastic and protomylonites as well as well-developed core and mantle structures in olivine-rich lenses in the mylonites (Figure 3e) indicate that grain size reduction in these rocks results essentially from subgrain rotation recrystallization.

[36] Deformation by dislocation creep is also inferred from the analysis of olivine and orthopyroxene CPO in all deformation facies, except the UMB. These CPO are consistent with dominant activation of the (010)[100] and (100)[001] slip systems in olivine and orthopyroxene, respectively [*Tommasi et al.*, 2000]. Variations of olivine CPO symmetry across the shear zone from axial-[010] patterns in the coarse porphyroclastic peridotites of the central domain to orthorhombic or even axial-[100] patterns in the mylonites may result from a variation in deformation regime (from transpression to simple shear [*Tommasi et al.*, 1999] or from a change in chemical environment (melt content, fH_20, fO_2) [*Bai et al.*, 1991; *Holtzman et al.*, 2003; *Mackwell et al.*, 1985]). Activation of multiple systems of the [100]{0kl} family in olivine is also suggested by the higher frequency of low-angle misorientations with [0VW] rotation axes (Figures 9 and 10). Predominance of [010] rotation axes accommodating low-angle misorientations imply however a higher density of [100](001) dislocations stored in subgrain walls relatively to [100](010) ones. Such a discrepancy between olivine slip systems' relative activities inferred from the analysis of the CPO and from misorientations has been previously described in peridotites [e.g., *Dijkstra et al.*, 2002; *Soustelle et al.*, 2010]. We interpret it as indicating a limitation of the misorientation data: the most mobile dislocations that accommodate most strain are not necessarily the best preserved in subgrain boundaries. Deformation experiments in olivine crystals imply that a decrease in temperature should result in a change in the dominant slip direction in olivine from [100] to [001] [*Durham and Goetze*, 1977; *Bai et al.*, 1991; *Tommasi et al.*, 2009]. Variations in olivine CPO consistent with such an inversion in the dominant glide direction of olivine are however not observed in the northern Lanzo shear zone. We propose that dominant activation of the high-temperature, low-pressure [100](010) slip system for olivine even in low-temperature mylonites and in the ultramylonite bands, results from control of the initial high-temperature olivine CPO on the subsequent deformation, that is, from plastic anisotropy [*Tommasi and Vauchez*, 2001; *Michibayashi and Mainprice*, 2004; *Tommasi et al.*, 2009].

[37] Dynamic recrystallization does not change the olivine CPO patterns (Figure 5), but results in dispersion that increases with increasing recrystallized matrix volume (Figure 7). Random olivine CPOs are however never observed, not even in the ultramylonitic bands. Thus it although dynamic recrystallization produces a grain size reduction by two orders of magnitude from the coarse-grained porphyroclastic peridotites to the mylonites, this change in microstructure does not result in a change in deformation mechanism, nor in the dominant slip systems for olivine and pyroxenes. Clinopyroxene and plagioclase CPO are usually weak and not consistent with the olivine and orthopyroxene CPO in the porphyroclastic peridotites, suggesting postkinematic crystallization due to melt-rock interaction. CPO of all phases are however correlated in most protomylonites and mylonites, indicating that the mylonitic deformation continued in the plagioclase stability field under subsolidus conditions.

[38] A different evolution is inferred for the mm-scale fine-grained and ultramylonitic bands that record the latest stages of deformation in the shear zone. Their microstructure (intermixed assemblages with interpenetrating grain boundaries, Figures 3f, 3h, 4b, and 4d) suggests that the extreme grain size reduction in these bands results from reactions rather than mechanical processes. This interpretation is corroborated by the observation of polymineralic coronas with similar compositions and textures surrounding the porphyroclasts (Figure 3h). Similar microstructures in ultramylonites in the Hidaka (Japan) and Pyrenees (France) massifs have also been interpreted as produced by syntectonic continuous net transfer solid-state reactions associated to the spinel to plagioclase-lherzolite transition [*Furusho and Kanagawa*, 1999; *Newman et al.*, 1999].

[39] A reactional origin for the polyphase domains in the ultramylonitic bands is further corroborated by the crystallographic orientation relations between the different phases composing a domain. The

similarity between amphibole and clinopyroxene CPO (Figure 8), together with their spatial association, suggest oriented growth of amphibole at the expenses of clinopyroxene during hydration reactions. Higher amphibole contents in the ultramylonite bands relatively to the other deformation facies together with the undeformed aspect of clinopyroxene-amphibole aggregates (Figure 4d) suggest channeling of late fluid percolation in these fine-grained bands. Orientation relations that cannot be explained by a common deformation are also observed between olivine and orthopyroxene. In the ultramylonite bands, orthopyroxene [001] axes are perpendicular to the foliation and parallel to the olivine [010] axes (Figure 8). The orthopyroxene CPO are not consistent with dislocation glide on usual (100)[001] system [*Mercier*, 1985], which activation is nevertheless suggested by the weak predominance of rotation axes accommodating low-angle misorientations in orthopyroxene close to [010] (Figure 9). Based on these observations, we propose that the orthopyroxene CPO is largely inherited from the olivine one.

[40] The close spatial relation between reactions and deformation (Figure 3) indicates that deformation plays an important role in the reaction kinetics. Reactions are favored in domains where dynamic recrystallization already reduced grain sizes, allowing for larger contact area [*Newman and Drury*, 2010]. Mechanical energy associated with deformation may also work as a catalyzer for the reactions [e.g., *Brodie*, 1980]. On the other hand, the extreme grain size reduction produced by the reactions probably resulted in a change in the rate-controlling deformation mechanism in these mm-scale bands, allowing for activation of grain boundary sliding, as suggested by the observation of planar grain boundaries parallel to the bands' trend (Figure 3f). Yet, the observed olivine CPOs that, although very weak, are similar to olivine CPO in the coarser-grained domains of the shear zone (Figure 8) together with the clear SPOs (Figures 3f, 3h, 4b, 4d, 6d, and 6e) suggest that dislocation creep played a significant role on the deformation within these bands. An alternative interpretation, favored by *Newman et al.* [1999] is that grain elongation resulted essentially from diffusional processes. In this case, observed olivine CPO might have been inherited from previous deformation stages.

[41] Altogether, microstructural observations in these ultramylonitic bands are consistent with reaction-induced softening, where development of very fine grained polymineralic aggregates by synkinematic reactions associated with retrogressive pressure and temperature conditions allowed for continued deformation in a very localized manner during the latest stages of the shear zone evolution [e.g., *Jaroslow et al.*, 1996; *Newman et al.*, 1999; *Dijkstra et al.*, 2004].

5.3. Strain Localization in the Lithospheric Mantle

[42] Most peridotite massifs and ophiolites are, like the major part of the Lanzo massif, characterized by coarse-grained porphyroclastic or granular textures to which are associated strong olivine CPO, implying that homogeneous deformation predominates in the upper mantle. Large-scale mylonitic shear zones were nevertheless mapped in some orogenic massifs, like Ronda and Beni Bousera in the Betic-Rifean belt (S Spain–N Morocco), Erro-Tobio in the Alps, and Turon de Tecouere in the Pyrenees, and in the Othris, Voltri, and Oman ophiolites (cf. review by *Dijkstra et al.* [2004]). A common characteristic of these mylonitic zones, shared by the northern Lanzo shear zone, is that they record an evolution under variable pressure and temperature conditions, associated to mantle exhumation in response to lithospheric thinning in extensional settings (orogenic massifs) or obduction (ophiolites).

[43] The northern Lanzo shear zone records progressive strain localization through time and space. Shearing in the hotter footwall was initially homogeneously distributed in a ≥1.5 km wide shear zone characterized by a homogeneous strain distribution (the present-day exposure probably only represents part of the initial high-temperature shear zone). In contrast, in the latest and shallowest stages, deformation is focused in a 100–150 m wide band along the northern border of the shear zone that is characterized by a highly heterogeneous strain distribution, where an anastomozed network of mm-scale ultramylonite bands accommodates most strain (Figure 2).

[44] The microstructures of the coarse porphyroclastic peridotites in the southwestern domain of the shear zone indicate deformation in presence of small melt fractions. These rocks display homogeneous deformation, consistent with a low strength. One may question which processes allowed for strain localization under such conditions. Since the strength of partially molten mantle rocks is strongly dependent on the melt fraction [*Hirth and Kohlstedt*, 1995a, 1995b], lateral variations in melt fraction might produce strain localization. Feedback

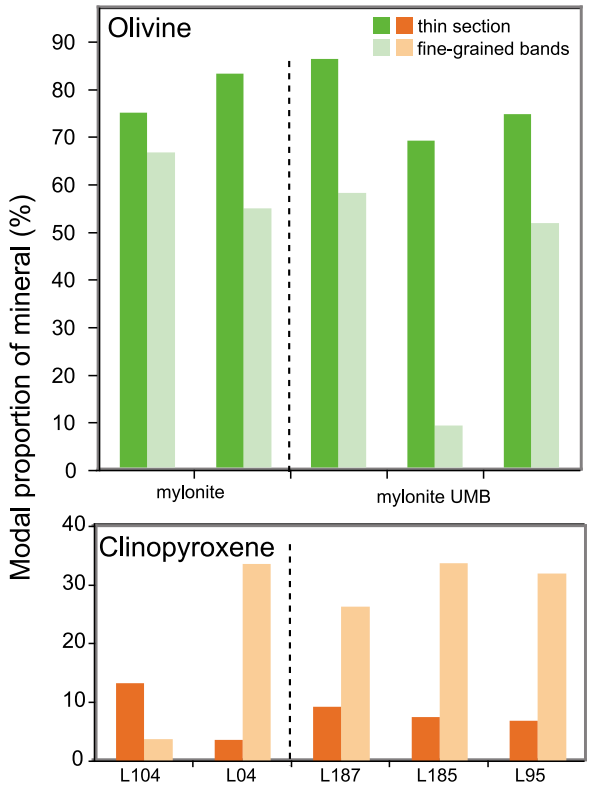

Figure 11. Comparison of the modal proportion (%) of olivine (green) and clinopyroxene (orange) in the entire thin section and in fine-grained bands in five samples.

between deformation and melt transport probably led to focusing of melt in the shear zone [e.g., *Tommasi et al.*, 1994; *Kelemen and Dick*, 1995; *Rosenberg and Handy*, 2000; *Holtzman et al.*, 2003; *Le Roux et al.*, 2008], as indicated by the more fertile (clinopyroxene-rich) composition of the mylonites (Figure 11).

[45] A close relation between petrological processes and strain localization is also inferred for the ultramylonite bands. Continuous net transfer solid-state reactions due to deformation under decreasing pressure-temperature conditions result in formation of very fine grained polyphase aggregates. These reactions take place preferentially in domains that have already fine-grained textures and are probably catalyzed by deformation. The micron-scale grain sizes in these bands, which may be maintained for long time spans due to their polyphase nature, allow for activation grain boundary sliding, indicated by the development of planar grain boundaries aligned parallel to the ultramylonite bands trend (Figures 3f and 3h). Effective strain localization due to this process may be inferred from the good preservation of microstructures characteristic of the previous deformation history in lenses between the UMB network (Figures 2, 3e, and 3g). Given the small dimensions of these ultramylonite bands that are in average 1 mm wide, one may however question if this process may accommodate large displacement gradients. Actual shear strain in these ultramylonite bands cannot be estimated, but even if a shear strain of 50 is considered, the relative displacement across a single ultramylonite band is of 50 mm. The ultramylonite bands represent in average 30% of the rock (Figure 2), implying that if shear strains of 50 are attained in these ultramylonite bands the total displacement across the 150 m wide low-temperature shear zone is on the order of 2.5 km.

[46] In contrast, the present observations indicate that grain size reduction by dynamic recrystallization does not result in a change in dominant deformation mechanism. Microstructures in the fine-grained porphyroclastic peridotites, protomylonites, and mylonites (except for the fine-grained bands) are consistent with deformation by dislocation creep with dominant activation of the high-temperature, low-pressure [100](010) and [001](100) slip systems for olivine and orthopyroxene, respectively. We propose that, in these intermediate domains, it is not the change in the microstructure that produces strain localization. Strain localization here results from external parameters: the more localizing behavior of the deeper and shallower parts of the shear zone discussed above that control the location of the fault, and by the need to deform a rock volume which strength continuously increases due to decreasing temperature conditions. The grain size decrease is rather a consequence of the focusing of the deformation in response to the strength variation.

5.4. An Extensional Shear Zone in the Mantle

[47] The present-day steeply dipping foliations and subhorizontal lineations in the northern Lanzo shear zone are more consistent with strike-slip deformation. The thermomechanical evolution of this shear zone is however characterized by deformation under decreasing temperature and pressure conditions, implying a vertical displacement component. This evolution is in better agreement with the one expected in a normal or detachment fault, where shearing results in faster exhumation rates in the footwall (central domain) relatively to the hanging wall (northern domain). The asymmetric structure of the northern Lanzo shear zone, marked by a progressive strain localization toward the

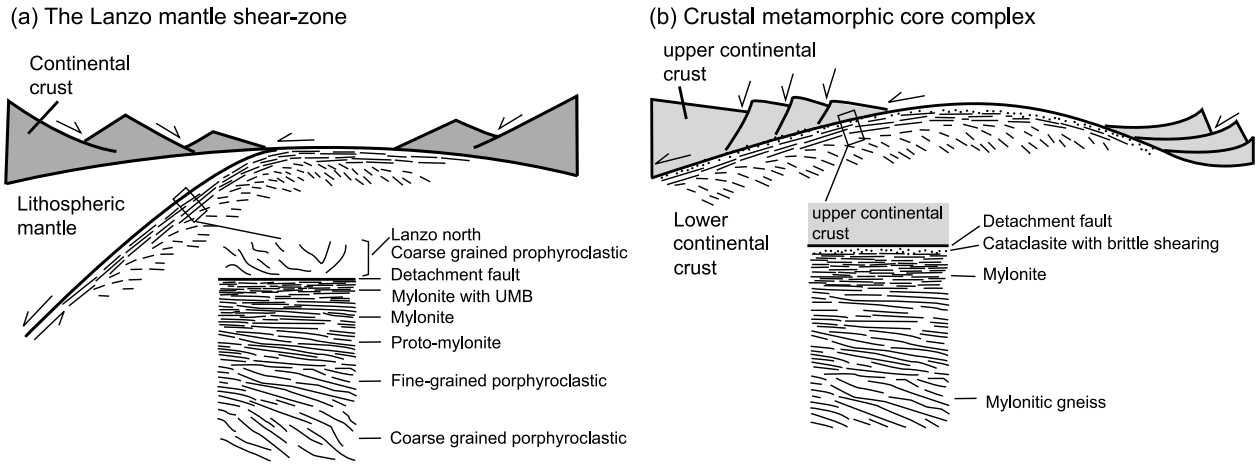

Figure 12. Schematic comparison between a detachment fault limiting a crustal metamorphic core complex and the Lanzo mantle shear zone. The detachment fault sketch is based on *Twiss and Moores* [2007], *Buck* [1990], *Reynolds and Lister* [1990], and M. Krabbendam and B. W. D. Yardley (Metamorphic core complex: Lower plate, footwall, upper plate, hangingwall, Figure 1., younger, and, Continental extensional tectonics, 2010, available at http://science.jrank.org/pages/47851/metamorphic-core-complex.html). Note the similar asymmetry of the structures and the progressive localization of deformation as it affects cooler and probably shallower mantle rocks that form the hanging wall of the shear zone.

cooler limit of the shear zone shows a striking similarity with the gradation in deformation facies from mylonites to cataclasites characteristic of the crustal detachment faults that border metamorphic core complexes (Figure 12). In both cases, exhumation and cooling of the footwall results in progressive strain localization. Structural levels and temperature conditions and hence deformation mechanisms implied in metamorphic core complexes' detachment faults and the northern Lanzo shear zone are however different. Crustal detachment faults develop as middle crustal rocks are exhumed to the surface by tectonic unroofing in an extensional setting and are characterized from a gradation from ductile to brittle deformation and the fault width usually varies from hundreds of meters for its ductile part to a few meters in the latest, brittle stages [*Coney*, 1980; *Davis*, 1988; *Reynolds and Lister*, 1990; *Buck*, 1991]. In contrast, all deformation is accommodated by viscoplastic (ductile) processes in the northern Lanzo shear zone and shearing is distributed over a wider domain (ranging from >1 km to ~150 m).

[48] The inconsistency between the present-day orientation and the observed pressure-temperature evolution of the shear zone might result from a solid rotation during the latest stages of exhumation of the massif and its emplacement within the crust. The distribution of mafic dykes and the geochemistry of the Lanzo peridotite [*Lagabrielle et al.*, 1990; *Pelletier and Müntener*, 2006; *Kaczmarek et al.*, 2008] suggests an original polarity where the southern and central domains have an asthenospheric history and the northern block a lithospheric one. This study indicates therefore that the northern Lanzo shear zone represents the deep section of a mantle detachment fault, corroborating previous models that proposed that it accommodated exhumation of the mantle in an ocean-continent transition zone or an (ultra)slow spreading ridge [*Kaczmarek and Müntener*, 2008, Figure 15], during the opening of the Piemont-Ligurian ocean.

6. Conclusions

[49] The Lanzo northern shear zone displays characteristics of an extensional shear zone, such as an asymmetric distribution of deformation facies and faster exhumation rates in the footwall (central block) relatively to the hanging wall (northern block). The gradient of deformation facies is consistent with deformation under continuously decreasing temperature conditions. Shearing started under near solidus conditions, close to the lithosphere-asthenosphere boundary. Strain localization during the early stages of deformation might have been controlled by feedback between deformation and melt transport, where concentration of melt in the higher-permeability shear zone lead to further strain localization. Exhumation and cooling of the footwall resulted in progressive strain localization toward the northern (upper) limit of the shear

zone, allowing the preservation of deformation microstructures formed at different structural levels. The latest stages of deformation are recorded by an anastomozed network of mm-scale ultramylonite bands concentrated along the northeastern limit of the shear zone.

[50] Grain size reduction by dynamic recrystallization does not result in a change in dominant deformation mechanism. All deformation facies (fine-grained bands excepted) display microstructures and CPO consistent with deformation by dislocation creep with dominant activation of the high-temperature, low-pressure [100](010) and [001](100) slip systems for olivine and orthopyroxene, respectively. We propose that it is not the change in the microstructure that produces strain localization in these intermediate levels, but that the microstructure evolves in response to strain focusing due to strength increase of the mantle as it is exhumed in the shear zone. Strain distribution at these levels is probably controlled by the more localizing behavior of both deeper and shallower sections of the shear zone.

[51] A different evolution is inferred for mm-scale ultramylonitic bands. Grain size reduction by reactions rather than mechanical processes in these bands is corroborated by the epitaxial relations between amphibole and clinopyroxene or orthopyroxene and olivine CPO. These reactions produced very fine grained polyphase aggregates, allowing for activation grain boundary sliding in these ultramylonite bands. Weak CPO and SPO suggest nevertheless that dislocation creep still played a role in the deformation in these bands.

Acknowledgments

[52] We thank D. Mainprice for software for analyzing/plotting CPO data and A. Vauchez for discussions on the deformation facies distribution on shear zones with varying kinematics. Detailed reviews by J. Platt and P. Skemer and editorial comments by T. Becker improved the manuscript and are gratefully acknowledged. Thanks to F. Barou for help with the EBSD measurements on the Crystal Probe at Geosciences Montpellier and C. Nevado and D. Delmas for high-quality polished thin sections for EBSD measurements. M.-A.K.'s postdoctoral research in Montpellier was funded by the Institut National des Sciences de l'Univers, Centre National de la Recherche Scientifique (INSU, CNRS, France). M.-A.K. also thanks the Australian Research Council (grant DP0878453) for funding part of this research. The EBSD-SEM national facility in Montpellier is supported by the INSU, CNRS, and by the Conseil Régional Languedoc-Roussillon, France.

References

Austin, N. J., and B. Evans (2007), Paleowattmeters: A scaling relation for dynamically recrystallized grain size, *Geology*, *35*(4), 343–346, doi:10.1130/G23244A.1.

Bai, Q., S. J. Mackwell, and D. L. Kohlstedt (1991), High temperature creep olivine single crystals: 1. Mechanical results for buffered samples, *J. Geophys. Res.*, *96*, 2441–2463, doi:10.1029/90JB01723.

Bodinier, J. L., M. A. Menzies, and M. F. Thirlwall (1991), Continental to oceanic mantle transition—REE and Sr-Nd isotopic geochemistry of the Lanzo lherzolite massif, *J. Petrol., Special Volume 2*, 191–210.

Boudier, F. (1972), Relations lherzolites-gabbro-dunite dans le massif de Lanzo (Alpes Piémontaises): Exemple de fusion partielle, Ph.D. thesis, Nantes Univ., Nantes, France.

Boudier, F. (1978), Structure and petrology of the Lanzo peridotite massif (Piedmont Alps), *Mem. Geol. Soc. Am.*, *89*, 1574–1591, doi:10.1130/0016-7606(1978)89<1574:SAPOTL>2.0.CO;2.

Boudier, F., and A. Nicolas (1972), Fusion partielle gabbroique dans la lherzolite de Lanzo (Alpes Piémontaises), *Bull. Suisse Mineral. Petrogr.*, *52*(1), 39–56.

Braun, J., J. Chéry, A. N. B. Poliakov, D. Mainprice, A. Vauchez, A. Tommasi, and M. Daignières (1999), A simple parameterization of strain localization in the ductile regime due to grain size reduction: A case study for olivine, *J. Geophys. Res.*, *104*(B11), 25,167–25,181, doi:10.1029/1999JB900214.

Brodie, K. H. (1980), Variations in mineral chemistry across a shear zone in phlogopite peridotite, *J. Struct. Geol.*, *2*(1–2), 265–272, doi:10.1016/0191-8141(80)90059-0.

Brown, M., and G. S. Solar (1998), Shear-zone systems and melts: Feedback relations and self-organization in orogenic belts, *J. Struct. Geol.*, *20*(2–3), 211–227, doi:10.1016/S0191-8141(97)00068-0.

Buck, W. R. (1990), Comment on "Origin of regional, rooted low-angle normal faults: A mechanical model and its tectonic implications," *Tectonics*, *9*(3), 545–546, doi:10.1029/TC009i003p00545.

Buck, W. R. (1991), Modes of continental lithospheric extension, *J. Geophys. Res.*, *96*(B12), 20,161–20,178, doi:10.1029/91JB01485.

Bunge, H. J. (1982), *Texture Analysis in Materials Sciences*, Butterworth, London.

Compagnoni, R., and R. Sandrone (1979), Il massicio di Lanzo nel quadro del metamorphismo alpino, *Soc. Ital. Mineral. Petrol.*, *35*(2), 842.

Coney, P. J. (1980), Metamorphic core complexes: An overview, *Mem. Geol. Soc. Am.*, *153*, 7–31.

Davis, G. A. (1988), Rapid upward transport of midcrustal mylonitic gneisses in the footwall of a Tertiary detachment fault, Whipple mountains, southeastern California, *Geol. Rundsch.*, *77*, 191–209, doi:10.1007/BF01848684.

Dijkstra, H. A., M. R. Drury, R. L. M. Vissers, and J. Newman (2002), On the role of melt-rock reaction in mantle shear zone formation in the Othris peridotite massif (Greece), *J. Struct. Geol.*, *24*, 1431–1450, doi:10.1016/S0191-8141(01)00142-0.

Dijkstra, A., M. R. Drury, R. L. M. Vissers, J. Newman, and H. L. M. Van Roermund (2004), Shear zones in the upper mantle: Evidence from alpine and ophiolite-type peridotite massifs, in *Flow Processes in Faults and Shear Zones*, edited by G. I. Alsop et al., *Geol. Soc. Spec. Publ.*, *224*, 11–24.

Dunbar, J. A., and D. S. Sawyer (1989), How preexisitng weakness control the style of continental breakup, *J. Geophys. Res.*, *94*, 7278–7292, doi:10.1029/JB094iB06p07278.

Durham, W. B., and G. Goetze (1977), Plastic flow of oriented single crystals of olivine: 1. Mechanical data, *J. Geophys. Res.*, *82*, 5737–5753, doi:10.1029/JB082i036p05737.

Furusho, M., and K. Kanagawa (1999), Transformation-induced strain localization in a lherzolite mylonite from the Hidaka metamorphic belt of the central Hokkaido, Japan, *Tectonophysics*, *313*, 411–432, doi:10.1016/S0040-1951(99)00215-2.

Herwegh, M., A. Berger, and A. Ebert (2005), Grain coarsening maps: A new tool to predict microfabric evolution of polymineralic rocks, *Mem. Geol. Soc. Am.*, *33*(10), 801–804.

Hirth, G., and D. L. Kohlstedt (1995a), Experimental constraints on the dynamics of the partially molten upper mantle: Deformation in the diffusion creep regime, *J. Geophys. Res.*, *100*(B2), 1981–2001, doi:10.1029/94JB02128.

Hirth, G., and D. L. Kohlstedt (1995b), Experimental constraints on the dynamics of the partially molten upper mantle: Deformation in the dislocation creep regime, *J. Geophys. Res.*, *100*(B8), 15,441–15,449, doi:10.1029/95JB01292.

Holtzman, B. K., and D. L. Kohlstedt (2007), Stress-driven melt segregation and strain partitioning in partially molten rocks: Effects of stress and strain, *J. Petrol.*, *48*(12), 2379–2406, doi:10.1093/petrology/egm065.

Holtzman, B. K., D. L. Kohlstedt, M. E. Zimmerman, F. Heidelbach, T. Hiraga, and J. Hustoft (2003), Melt segregation and strain partitioning: Implications for seismic anisotropy and mantle flow, *Science*, *301*, 1227–1230, doi:10.1126/science.1087132.

Jaroslow, G. E., G. Hirth, and H. J. B. Dick (1996), Abyssal peridotite mylonites: Implications for grain-size sensitive flow and strain localization in the oceanic lithosphere, *Tectonophysics*, *256*, 17–37, doi:10.1016/0040-1951(95)00163-8.

Kaczmarek, M.-A., and O. Müntener (2008), Juxtaposition of melt impregnation and high temperature shear zone in the upper mantle: Field and petrological constraints from the Lanzo peridotite (N-Italy), *J. Petrol.*, *49*(12), 2187–2220, doi:10.1093/petrology/egn065.

Kaczmarek, M.-A., and O. Müntener (2010), The variability of peridotite composition across a mantle shear zone (Lanzo massif, Italy): Interplay of melt focusing and deformation, *Contrib. Mineral. Petrol.*, *160*, 663–679, doi:10.1007/s00410-010-0500-8.

Kaczmarek, M.-A., O. Müntener, and D. Rubatto (2008), Trace element chemistry and U-Pb dating of zircons from oceanic gabbros and their relationship with whole rock composition (Lanzo, Italian Alps), *Contrib. Mineral. Petrol.*, *155*, 295–312, doi:10.1007/s00410-007-0243-3.

Kelemen, P. B., and H. J. B. Dick (1995), Focused melt flow and localized deformation in the upper mantle: Juxtaposition of replacive dunite and ductile shear zones in the Josephine peridotite, SW Oregon, *J. Geophys. Res.*, *100*(B1), 423–438, doi:10.1029/94JB02063.

Kienast, J. R., and U. Pognante (1988), Chloritoid-bearing assemblages in eclogitized metagabbros of the Lanzo peridotite body (western Italian Alps), *Lithos*, *21*(1), 1–11, doi:10.1016/0024-4937(88)90002-3.

Lagabrielle, Y., S. Fudral, and J.-R. Kienast (1990), La couverture océanique des ultrabasites de Lanzo (Alpes Occidentales): Arguments lithostratigraphiques et pétrologiques, *Geodin. Acta*, *4*(1), 43–55.

Lapierre, J., W. Ben Ismaïl, and D. Mainprice (1996), A method to calculate rock physical properties from published pole figures, in *Structural Geology and Personal Computers. Computer Methods in Geosciences*, edited by D. Paor, pp. 167–178, Pergamon, Oxford, U. K., doi:10.1016/S1874-561X(96)80015-0.

Le Roux, V., A. Tommasi, and A. Vauchez (2008), Feedback between melt percolation and deformation in an exhumed lithosphere-asthenosphere boundary, *Earth Planet. Sci. Lett.*, *274*(3–4), 401–413, doi:10.1016/j.epsl.2008.07.053.

Mackwell, S. J., D. Kohlstedt, and M. Paterson (1985), Role of water in the deformation of olivine single-crystals, *J. Geophys. Res.*, *90*, 11,319–11,333, doi:10.1029/JB090iB13p11319.

Mercier, J.-C. (1985), Olivine and pyroxene, in *Preferred Orientation in Deformed Metals and Rocks: An Introduction to Modern Texture Analysis*, edited by H. R. Wenk, pp. 407–430, Academic, Orlando, Fla.

Michibayashi, K., and D. Mainprice (2004), The role of preexisting mechanical anisotropy on shear zone development within oceanic mantle lithosphere: An example from the Oman Ophiolite, *J. Petrol.*, *45*(2), 405–414, doi:10.1093/petrology/egg099.

Müntener, O., and G. B. Piccardo (2003), Melt migration in ophiolitic peridotites: The message from Alpine-Apennine peridotites and implications for embryonic ocean basins, in *Ophiolites in Earth History*, edited by Y. Dilek and P. T. Robinson, *Geol. Soc. Spec. Publ.*, *218*, 69–89.

Neves, S. P., A. Tommasi, A. Vauchez, and R. Hassani (2008), Intraplate continental deformation: Influence of a heat production layer in the lithospheric mantle, *Earth Planet. Sci. Lett.*, *274*(3–4), 392–400, doi:10.1016/j.epsl.2008.07.040.

Newman, J., and M. R. Drury (2010), Control of shear zone location and thickness by initial grain size variations in upper mantle peridotites, *J. Struct. Geol.*, *32*, 832–842, doi:10.1016/j.jsg.2010.06.001.

Newman, J., W. M. Lamb, M. R. Drury, and R. L. M. Vissers (1999), Deformation processes in a peridotite shear zone: Reaction-softening by an H_2O-deficient, continuous net transfer reaction, *Tectonophysics*, *303*, 193–222, doi:10.1016/S0040-1951(98)00259-5.

Nicolas, A. (1968), Relations structurales entre le massif ultrabasique de Lanzo, ses satellites et la zone de Sesia Lanzo, in *Symposium 'Zone Ivrea-Verbano,'* vol. 48, pp. 145–156, Verlag Leemann, Zurich, Switzerland.

Nicolas, A., and J.-P. Poirier (1976), *Crystalline Plasticity and Solid State Flow in Metamorphic Rocks*, John Wiley, New York.

Niida, K., and D. H. Green (1999), Stability and chemical composition of pargasitic amphibole in MORB pyrolite under upper mantle conditions, *Contrib. Mineral. Petrol.*, *135*, 18–40, doi:10.1007/s004100050495.

Pelletier, L., and O. Müntener (2006), High pressure metamorphism of the Lanzo peridotite and its oceanic cover, and some consequences for the Sesia-Lanzo zone (northwestern Italian Alps), *Lithos*, *90*, 111–130, doi:10.1016/j.lithos.2006.01.006.

Piccardo, G. B., A. Zanetti, and O. Müntener (2007a), Melt/peridotite interaction in the Southern Lanzo peridotite: Field, textural and geochemical evidence, *Lithos*, *94*(1–4), 181–209, doi:10.1016/j.lithos.2006.07.002.

Piccardo, G. B., A. Zanetti, A. Pruzzo, and M. Padovano (2007b), The North Lanzo peridotite body, (NW Italy): Lithospheric mantle percolated by MORB and alkaline melts, *Period. Mineral.*, *76*, 175–196.

Poirier, J.-P. (1980), Shear localization and shear instability in materials in the ductile field, *J. Struct. Geol.*, *2*(1–2), 135–142, doi:10.1016/0191-8141(80)90043-7.

Précigout, J., F. Gueydan, D. Gapais, C. J. Garrido, and A. Essaifi (2007), Strain localisation in the subcontinental mantle—A ductile alternative to the brittle mantle, *Tectonophysics*, *445*, 318–336, doi:10.1016/j.tecto.2007.09.002.

Randle, V. (1992), *Microtexture Determination and Its Applications*, Inst. of Mater., London.

Regenauer-Lieb, K., and D. A. Yuen (2003), Modeling shear zones in geological and planetary sciences: Solid- and fluid-thermal-mechanical approaches, *Earth Sci. Rev.*, *63*(3–4), 295–349, doi:10.1016/S0012-8252(03)00038-2.

Reynolds, S. J., and G. S. Lister (1990), Folding of mylonitic zones in Cordilleran metamorphic core complexes: Evidence from near the mylonitic front, *Geology*, *18*(3), 216–219, doi:10.1130/0091-7613(1990)018<0216:FOMZIC>2.3.CO;2.

Rosenberg, C., and M. R. Handy (2000), Syntectonic melt pathways during simple shearing of a partially molten rock analogue (Norcamphor-Benzamide), *J. Geophys. Res.*, *105*(B2), 3135–3149, doi:10.1029/1999JB900371.

Skemer, P., J. M. Warren, P. B. Kelemen, and G. Hirth (2010), Microstructural and rheological evolution of a mantle shear zone, *J. Petrol.*, *51*, 43–53, doi:10.1093/petrology/egp057.

Soustelle, V., A. Tommasi, J. L. Bodinier, C. Garrido, and A. Vauchez (2009), Deformation and reactive melt transport in the mantle lithosphere above a large-scale partial melting domain: The Ronda peridotite massif, southern Spain, *J. Petrol.*, *50*(7), 1235–1266, doi:10.1093/petrology/egp032.

Soustelle, V., A. Tommasi, S. Demouchy, and D. A. Ionov (2010), Deformation and fluid-rock interaction in the supra-subduction mantle: Microstructures and water contents in the peridotite xenoliths from the Avacha volcano, Kamchatka, *J. Petrol.*, *51*(1–2), 363–394, doi:10.1093/petrology/egp085.

Stünitz, H., and J. Tullis (2001), Weakening and strain localization produced by syn-deformational reaction of plagioclase, *Int. J. Earth Sci.*, *90*(1), 136–148, doi:10.1007/s005310000148.

Tommasi, A., and A. Vauchez (2001), Continental rifting parallel to ancient collisional belts: An effect of the mechanical anisotropy of the lithospheric mantle, *Earth Planet. Sci. Lett.*, *185*, 199–210, doi:10.1016/S0012-821X(00)00350-2.

Tommasi, A., A. Vauchez, L. A. D. Fernandes, and C. C. Porcher (1994), Orogen-parallel strike-slip faulting and synkinematic magmatism in the Dom Feliciano Belt, southern Brazil, *Tectonics*, *13*, 421–437, doi:10.1029/93TC03319.

Tommasi, A., A. Vauchez, and B. Daudre (1995), Initiation and propagation of shear zones in a heterogeneous continental lithosphere, *J. Geophys. Res.*, *100*, 22,083–22,101, doi:10.1029/95JB02042.

Tommasi, A., B. Tikoff, and A. Vauchez (1999), Upper mantle tectonics: Three-dimensional deformation, olivine crystallographic fabrics and seismic properties, *Earth Planet. Sci. Lett.*, *168*, 173–186, doi:10.1016/S0012-821X(99)00046-1.

Tommasi, A., D. Mainprice, G. Canova, and Y. Chastel (2000), Viscoplastic self-consistent and equilibrium-based modeling of olivine lattice preferred orientations: Implications for the upper mantle seismic anisotropy, *J. Geophys. Res.*, *105*(B4), 7893–7908, doi:10.1029/1999JB900411.

Tommasi, A., M. Knoll, A. Vauchez, J. W. Signorelli, C. Thoraval, and R. Logé (2009), Structural reactivation in plate tectonics controlled by olivine crystal anisotropy, *Nat. Geosci.*, *2*, 423–427, doi:10.1038/ngeo528.

Twiss, R. J., and E. M. Moores (2007), *Structural Geology*, 2nd ed., W. H. Freeman, New-York.

Vauchez, A., and A. Tommasi (2003), Wrench faults down to the asthenosphere: Geological and geophysical evidence and thermo-mechanical effects, in *Intraplate Strike-Slip Deformation Belts*, edited by F. Storti et al., *Spec. Publ. Geol. Soc.*, *210*, 15–34.

Vauchez, A., S. P. Neves, R. Caby, M. Corsini, M. Egydio-Silva, M. Arthaud, and V. E. Amaro (1995), The Borborema shear zone system, *J. South Am. Earth Sci.*, *8*, 247–266, doi:10.1016/0895-9811(95)00012-5.

Vauchez, A., F. Dineur, and R. Rudnick (2005), Microstructure, texture and seismic anisotropy of the lithospheric mantle above a mantle plume: Insights from the Labait volcano xenoliths (Tanzania), *Earth Planet. Sci. Lett.*, *232*, 295–314, doi:10.1016/j.epsl.2005.01.024.

Vissers, R. L. M., M. R. Drury, E. H. Hoogerduijn Strating, C. J. Spiers, and D. Van der Wal (1995), Mantle shear zone and their effect on lithosphere strength during continental break-up, *Tectonopysics*, *249*, 155–171.

Wheeler, J., D. J. Prior, Z. Jiang, R. Spiess, and P. W. Trimby (2001), The petrological significance of misorientations between grains, *Contrib. Mineral. Petrol.*, *141*(1), 109–124, doi:10.1007/s004100000225.

White, S. H., S. E. Burrows, J. Carreras, N. D. Shaw, and F. J. Humphreys (1980), On mylonite in ductile shear zone, *J. Struct. Geol.*, *2*(1–2), 175–187, doi:10.1016/0191-8141(80)90048-6.